Biomech Model Mechanobiol (2017) 16:1779–1803
DOI 10.1007/s10237-017-0919-1

ORIGINAL PAPER

A patient-specific aortic valve model based on moving resistive immersed implicit surfaces

Marco Fedele[1,2] · **Elena Faggiano**[1,2] · **Luca Dedè**[1,3] · **Alfio Quarteroni**[1,3]

Received: 7 June 2016 / Accepted: 12 May 2017 / Published online: 7 June 2017

Abstract In this paper, we propose a full computational framework to simulate the hemodynamics in the aorta including the valve. Closed and open valve surfaces, as well as the lumen aorta, are reconstructed directly from medical images using new ad hoc algorithms, allowing a patient-specific simulation. The fluid dynamics problem that accounts from the movement of the valve is solved by a new 3D–0D fluid–structure interaction model in which the valve surface is implicitly represented through level set functions, yielding, in the Navier–Stokes equations, a resistive penalization term enforcing the blood to adhere to the valve leaflets. The dynamics of the valve between its closed and open position is modeled using a reduced geometric 0D model. At the discrete level, a finite element formulation is used and the SUPG stabilization is extended to include the resistive term in the Navier–Stokes equations. Then, after time discretization, the 3D fluid and 0D valve models are coupled through a staggered approach. This computational framework, applied to a patient-specific geometry and data, allows to simulate the movement of the valve, the sharp pressure jump occurring across the leaflets, and the blood flow pattern inside the aorta.

Keywords Aortic valve · Image-based modeling · Patient-specific simulation · Computational fluid dynamics · Finite element method · Heart modeling

1 Introduction

In the context of computational fluid dynamics for the cardiovascular system (see, e.g., Quarteroni 2015; Formaggia et al. 2010; Peskin 2002), patient-specific simulations have become increasingly important (Caballero and Laín 2013; Taylor and Steinman 2010): indeed, they can be used together with classical imaging methods to perform diagnosis, to provide more insights in the study of the evolution of pathologies, or to help in surgical procedure planning, e.g., to virtually create alternative treatment strategies for a given patient.

In the whole cardiovascular system, the proximal aorta together with the aortic valve is likely the most investigated environment (Caballero and Laín 2013; Chandran and Vigmostad 2013; Faggiano et al. 2013a; Conti et al. 2010a; Pasta et al. 2013; Marom et al. 2013; Tse et al. 2011; Rinaudo and Pasta 2014; Wendell et al. 2013). The aorta is the main artery of the human body suppling oxygenated blood and nutrients to all the components of the body. It originates from the left ventricle of the heart and extends down to the abdomen. In its first tract, it comprises the aortic root and the ascending aorta. The aortic root includes: (a) three enlargements, the so-called sinuses of Valsalva, classified as left coronary, right coronary and non-coronary sinuses, (b) the fibrous aortic annulus connecting the valve leaflets, the sinuses, and the ventricle, and (c) the sinotubular junction (STJ) representing the region where the normal tubular configuration of the aorta is attained. The left ventricle and the aortic root are separated by the aortic valve which features three thin and

✉ Elena Faggiano
elena.faggiano@unipv.it

1 CMCS - MATHICSE - SB, École Polytechnique Fédérale de Lausanne, Lausanne, Switzerland

2 Present Address: CompMech Group, Department of Civil Engineering and Architecture, University of Pavia, Pavia, Italy

3 MOX, Dipartimento di Matematica, Politecnico di Milano, Milan, Italy

flexible leaflets shaped as curved triangles and attached to the fibrous aortic annulus, forming with the latter a parabolic profile (Charitos and Sievers 2013). The efficient opening and closing of the aortic valve during the cardiac cycle guarantees the appropriate circulation of blood flow from the left ventricle to the ascending aorta, thus preventing regurgitation phenomena.

Other than focusing on the valve in physiological conditions, different studies were conducted to understand aortic pathologies; in this respect, we recall computational studies of aortic diseases due to bicuspid aortic valve (Chandran and Vigmostad 2013; Faggiano et al. 2013a; Vergara et al. 2012; Conti et al. 2010a; Pasta et al. 2013; Marom et al. 2013; Bonomi et al. 2015), computational investigations of valve prosthesis (Morganti et al. 2014; Auricchio et al. 2014, 2011; Hart et al. 2003a; Nestola et al. 2016), and aortic aneurysms or dissection studies (Tse et al. 2011; Rinaudo and Pasta 2014). Among these, some studies aim at understanding the valve mechanics with a particular interest for stresses internal to the valve leaflets and the aortic root (Morganti et al. 2014; Auricchio et al. 2011, 2014; Hart et al. 2003a; Marom et al. 2013; Conti et al. 2010b), while other studies focus on the fluid dynamics in the aorta investigating possible abnormalities trough appropriate indicators (Chandran and Vigmostad 2013; Faggiano et al. 2013a; Vergara et al. 2012; Conti et al. 2010a; Pasta et al. 2013; Tse et al. 2011; Rinaudo and Pasta 2014; Bonomi et al. 2015; Nestola et al. 2016). In this work, we introduce a numerical method able to capture the features of the blood flow through the first tract of the aorta. Since the flow field strongly depends on the aortic valve function, the latter should be necessarily included in our model. Indeed, the valve regulates the blood flow and plays an important role in both physiological and pathological scenarios.

Our model for the valve characterization involves a three-dimensional (3D) fluid–structure interaction (FSI) model accounting for the coupling between valve dynamics and blood flow. Computational methods for FSI simulations of aortic valve dynamics can be tentatively grouped into four categories: the approaches based on the so-called Arbitrary Lagrangian Eulerian (ALE) formulation (Chandra et al. 2012; Cheng et al. 2004; Marom et al. 2013), those based on the immersed boundary (IB) methods (Peskin 1972; McQueen and Peskin 2000; Griffith 2012), those based on fictitious domain (FD) formulations (Loon et al. 2006; Hart et al. 2003a, b, 2004), and those based on hybrid formulations (Ge and Sotiropoulos 2007; Borazjani et al. 2010; Ge and Sotiropoulos 2010; Le and Sotiropoulos 2013; Kamensky et al. 2015). All of them require a spatial discretization of the problem over a computational mesh. In the ALE formulation, the computational mesh is deformed to follow the boundaries of the fluid domain, in this case the aortic valve leaflets; however, this approach requires frequent remeshing of the domain to deal with large mesh deformation and involves topology changes when the valve opens and closes. In both IB and FD methods the fluid is instead discretized in a fixed computational domain, while the valve structure is discretized in a separate body-fitted mesh with the coupling accounted either explicitly or implicitly by adding suitable forces at the fluid/solid interface. In particular, for the IB method, the appropriate forces are explicitly added to the fluid equation and distributed over all nodes of the fluid mesh through a smoothed Dirac delta function (Peskin 1972, 2002). An evolution of the original method, in which the mesh is adaptively refined in the proximity of the immersed boundaries, was applied to aortic valve simulations in Griffith (2012). In the FD method the coupling between the fluid and the solid problem is made through Lagrange multipliers (Loon et al. 2006); the method had been applied to simulate a trileaflet aortic valve at non-physiological Reynolds numbers ($Re = 900$) and with symmetry assumption on the geometry (Hart et al. 2004, 2003a, b; Morsi et al. 2007). Finally, among the hybrid formulations, we recall the curvilinear immersed boundary (CURVIB) method developed by Ge and Sotiropoulos (2007) which integrates structured curvilinear boundary fitted grids with an IB method. The CURVIB method had been applied to study trileaflet and bileaflet aortic valves with physiological, pulsating flows, even if not in realistic aortas (Le and Sotiropoulos 2013; Ge and Sotiropoulos 2010; Borazjani 2013). Borazjani et al. (2010) tested the method in a patient-specific anatomic aorta, even if only a simple mechanical bileaflet valve has been simulated. Another recent method is the ALE/IB immersogeometric method proposed by Kamensky et al. (2015) and Hsu et al. (2014) which combines a variational IB method and the traditional ALE technique. The authors applied the method to a simplified aortic root geometry and valve leaflets demonstrating promising abilities of the proposed strategy (Hsu et al. 2014).

A major challenge in trileaflet aortic valve FSI simulations is to capture the coaptation between the leaflets of the valve during the closing phase. Most of the previous methods have circumvented this problem by allowing the valve to remain partially open (Kamensky et al. 2015; Hart et al. 2003b; Borazjani 2013). Astorino et al. (2009) introduced an algorithm for calculating self-contacts of thin structures inside a fluid domain using the FD formulation, which they applied to aortic valve simulations, even if only for small values of diastolic transvalvular pressure, specifically about 0.1 mmHg. Marom et al. (2012) have carried out 3D FSI simulations for an aortic valve with leaflet coaptation, by coupling a finite element (FE) commercial code for the mechanics of the leaflets with a commercial finite volume flow solver; however, only the final stages of the valve closure in a simplified geometry have been successfully simulated.

Several challenges arise when using full 3D FSI models. They regard high computational costs, handling of large

displacements of the valve leaflets in the aortic root, contact among the leaflets, and high pressure jumps across a closed or nearly closed valve. At the numerical level, highly accurate, stable, and robust spatial and time discretization schemes must be used. For these reasons, full 3D FSI models are nowadays mostly restricted to study valves in simplified configurations possibly with simplified flow assumptions or only with a simpler bileaflet mechanical valve. Indeed, to the best of our knowledge, a 3D FSI simulation with trileaflet aortic valve and patient-specific aortic and valve geometry has not been successfully pursuit yet.

Concerning the patient-specific studies of the fluid dynamics in the ascending aorta reported in the literature, a full model of the valve is not even considered when the focus is on valves pathologies (Faggiano et al. 2013a; Vergara et al. 2012; Della Corte et al. 2012; Pasta et al. 2013; Tse et al. 2011; Rinaudo and Pasta 2014; Bonomi et al. 2015; Nestola et al. 2016). Indeed, the valve is either completely neglected (Tse et al. 2011; Nestola et al. 2016), or included as an orifice at the inlet surface without the need of providing its detailed geometry (Faggiano et al. 2013a; Vergara et al. 2012; Wendell et al. 2013), or embedded as a set of fixed surfaces inside the aortic domain (Della Corte et al. 2012; Pasta et al. 2013; Rinaudo and Pasta 2014; Bonomi et al. 2015). In all these cases, the adopted model describes only the open and closed states of the valve without accounting for the intermediate positions between these two configurations. Nevertheless, most of the above mentioned papers highlight the importance of the inclusion of the valve in the model in terms of patient-specific valve orifice or in terms of patient-specific valve leaflets. In particular, Faggiano et al. (2013a), Vergara et al. (2012) and Wendell et al. (2013) showed that the inclusion of the shape of the valve orifice determines the correct flow pattern in the vessel, highlighting also the influence of the area of the orifice. Della Corte et al. (2012) stressed the importance to include the leaflets surfaces in the fluid simulations, reporting that cusp opening restrictions or asymmetries cause a modification to the physiological flow direction. A recent work of Bonomi et al. (2015) highlights—through simulations performed on the same aortic geometry—the importance of including complete valve leaflets in the model, even if kept fixed, for inducing the patient-specific pathological helical flow patterns in the aorta which otherwise could not have been fully reproduced, not even through the mere inclusion of the patient-specific shape of the valve orifice.

Based on the above considerations, we aim at providing a computational method to study and numerically simulate the fluid dynamics in the aorta including the valve leaflets and the aortic valve orifice for the whole cardiac cycle by means of a reduced FSI model for the characterization of the interaction between the blood flow and the valve leaflets. Specifically, we propose a new method for the representation of the valve leaflets, which we name resistive immersed implicit surface (RIIS) method. Indeed, our approach is based on the resistive immersed surface (RIS) approach, originally proposed in Fernández et al. (2008) to study a porous interface immersed in a fluid and lately extended in Astorino et al. (2012) to model the aortic valve. However, in the work of Astorino et al. (2012), the mechanics of the leaflets is neglected and the valve is replaced by two immersed surfaces fixed in space describing the open and the closed valve, respectively. The presence of two valve surfaces is taken into account in the momentum equation of the Navier–Stokes equations by adding a penalization term, specifically a resistive term, which weakly enforces the blood to adhere to the leaflets. In our approach, we extend the model of Astorino et al. (2012) representing the valve surfaces implicitly through a level set formulation for the leaflets. In this way, the immersed surfaces are described analytically, thus avoiding the need of discretizing them by a computational mesh. This newly proposed extension facilitates embedding the resistive method - firstly used for fixed valves in Astorino et al. (2012) - into the framework of a valve displacing under a prescribed motion law. The latter could be deduced from literature-based physiological data, from patient-specific clinical images, or determined by numerically solving a mechanical model of the leaflets. In this respect, the analytical description of the valve motion allows to track large displacements and large deformations of the leaflets, as those occurring in the aortic valve. Starting from this consideration, we propose to use our RIIS method in a 3D–0D FSI reduced model for the interactions between the fluid and the valve leaflets. We model the dynamics of the valve between its closed and open position using a 0D model proposed by Korakianitis and Shi (2006) based on a second-order ordinary differential equation (ODE) with the leaflets angle as the unique, dependent variable. In particular, the configuration of the valve leaflets at each time instant depends on the flow rate and the pressure field in the aorta and in the left ventricle as forcing terms of the 0D valve model. This is achieved through a reduced fully coupled 3D–0D FSI model where the Navier–Stokes equations for the blood flow are coupled to the ODE representing the valve dynamics. The leaflets position affects the momentum equation of the Navier–Stokes equations by means of the resistive term, for which the valve is described with implicit level set functions (RIIS); on the other side, the ODE describing the dynamics of the valve receives as input the pressure jump across the valve and the flow rate. Our reduced 3D–0D FSI model provides the motion of the orifice and of the leaflets position at a limited computational cost with respect to a full 3D FSI solver. Indeed, our model is solved in an Eulerian formulation and in a fixed computational domain. A similar resistive Eulerian surfaces framework was firstly proposed by Laadhari

and Quarteroni (2016). However, in our work we propose a significantly different algorithm to couple the 3D fluid and 0D valve models which allows to obtain realistic physiological results. For the numerical approximation of the Navier–Stokes equations with the RIIS formulation, we consider the FE method for which the approximate velocity and pressure variables are built from Lagrangian polynomial basis functions of the same degree. In order to obtain a stable formulation and to control numerical instabilities associated with the highly advective blood flow regime through the valve, we consider and extend for the first time the SUPG stabilization (Bazilevs et al. 2007; Forti and Dedè 2015) to the Navier–Stokes equations with RIIS in the framework of the variational multiscale method (VMS). Finally, in order to deal with patient-specific cases, we develop a full computational framework starting from medical images and ending with the numerical simulation results. In particular, we propose a technique to segment both the aorta and the leaflets from computed tomography images. The result of the segmentation of the aorta is then used to generate a computational mesh. Moreover, we propose a new interpolation strategy which allows to transform a point cloud description of the patient-specific leaflets in an implicit level set function to be used in the RIIS formulation, and to achieve the challenging goal of reconstructing patient-specific valve leaflets. We remark that a patient-specific test case is reproduced also in Astorino et al. (2012); the method proposed in Barber et al. (2007) was used to obtain a patient-specific volumetric mesh of the aortic root which includes the aortic valve in both the open and closed positions. Such reconstruction method is however not straightforward for pathological cases such as bicuspid valves (which comprise five different configurations), unicuspid aortic valves, or implanted valves in non-natural positions. Indeed, it would require to map a template mesh over the patient geometry possibly leading to degenerate meshes (Barber et al. 2007). Our approach intends to overcome this drawback by simplifying the reconstruction process of the leaflets with a method that is able to reproduce both physiological and pathological scenarios, the latter being the most interesting for clinicians. To summarize, the aim of this work is twofold: (1) propose a new method for blood flow simulation in the aortic root and aorta with the inclusion of the movement of the valve leaflets; (2) propose a computational framework that allows to simulate the hemodynamics in a patient-specific aorta by using patient-specific aortic valve leaflets.

The outline of the paper is as follows: in Sect. 2 the reduced 3D–0D FSI model for the aortic valve is mathematically described, while in Sect. 3 its numerical approximation is afforded; the generation of the aortic domain and the patient-specific leaflets is presented in Sect. 4. In Sect. 5, the whole framework is applied to a patient-specific dataset and numerical results on valve movement, pressure and velocity fields are reported; conclusions follow in Sect. 6.

2 Mathematical modeling

In this section, we describe the RIIS model, we adapt it to describe the fluid dynamics of the aortic valve (AV-RIIS model), we recall the 0D model based on ODEs proposed by Korakianitis and Shi (2006) to compute the aortic valve angle (AV-0D model), and finally we show our approach to couple the AV-0D and the AV-RIIS models into the 3D–0D FSI model for the aortic valve.

2.1 The resistive immersed implicit surface (RIIS) model

We describe the mathematical model adopted to represent a fluid in a general domain with an immersed surface into it. In particular, first we recall the RIS model (Fernández et al. 2008; Astorino et al. 2012), then we describe the surface through an implicit function, and finally we present our RIIS model.

Given a fixed domain $\Omega \subset \mathbb{R}^3$ and an immersed surface $\Gamma \subset \Omega$, the RIS model introduced by Fernández et al. (2008) consists in enriching the classical Navier–Stokes equations with a penalization term in the conservation momentum equation holding only on the immersed surface Γ. The RIS Eulerian formulation for a generic incompressible homogeneous Newtonian fluid reads: find the velocity $\boldsymbol{u}$ and the pressure p such that, for all $t \in (0, T)$:

$$\begin{cases} \rho \dfrac{\partial \boldsymbol{u}}{\partial t} - 2\mu \nabla \cdot \boldsymbol{D}(\boldsymbol{u}) + \rho(\boldsymbol{u} \cdot \nabla)\boldsymbol{u} \\ + \nabla p + \delta_\Gamma \boldsymbol{R}_{\Gamma,\varepsilon}(\boldsymbol{u} - \boldsymbol{u}_\Gamma) = \boldsymbol{f} & \text{in } \Omega \\ \nabla \cdot \boldsymbol{u} = 0 & \text{in } \Omega \end{cases} \tag{1}$$

endowed with suitable initial and boundary conditions. We indicate with ρ the density of the fluid, with μ its dynamic viscosity, and with $\boldsymbol{D}(\boldsymbol{u})$ the strain rate tensor

$$\boldsymbol{D}(\boldsymbol{u}) = \frac{\nabla \boldsymbol{u} + \nabla^T \boldsymbol{u}}{2}. \tag{2}$$

The corresponding Cauchy stress tensor, in case of Newtonian fluids, reads:

$$\boldsymbol{\sigma}(\boldsymbol{u}, p) = -p\boldsymbol{I} + 2\mu \boldsymbol{D}(\boldsymbol{u}), \tag{3}$$

where $\boldsymbol{I}$ is the identity tensor. The quantities δ_Γ, $\boldsymbol{R}_{\Gamma,\varepsilon}$ and $\boldsymbol{u}_\Gamma$, all referring to the immersed surface Γ, represent the "Dirac distribution" used to localize Γ in Ω, a symmetric and positive second-order tensor modeling its resistance, and the

velocity of Γ, respectively; at this stage, $\boldsymbol{u}_\Gamma$ has to be referred as a data for the fluid problem. For the sake of simplicity, we also assume that the boundary $\partial\Omega$ of the domain is divided into two non-overlapping subsets $\partial\Omega_D$ and $\partial\Omega_N$ such that $\partial\Omega = \partial\Omega_D \cup \partial\Omega_N$ where Dirichlet and Neumann boundary conditions are assigned:

$$\begin{aligned} \boldsymbol{u} &= \boldsymbol{g} \qquad \text{on } \partial\Omega_D \times (0,T), \\ \boldsymbol{\sigma}\boldsymbol{n} &= \boldsymbol{h} \qquad \text{on } \partial\Omega_N \times (0,T), \end{aligned} \tag{4}$$

respectively, for $\boldsymbol{g}$ and $\boldsymbol{h}$ given; problem (1) is endowed with the initial condition:

$$\boldsymbol{u}(\boldsymbol{x},0) = \boldsymbol{u}_0(\boldsymbol{x}) \qquad \text{in } \Omega, \tag{5}$$

for some initial velocity $\boldsymbol{u}_0$. The symmetric tensor $\boldsymbol{R}_{\Gamma,\varepsilon}$ was introduced in Fernández et al. (2008) to model fixed porous interfaces (for which $\boldsymbol{u}_\Gamma = \boldsymbol{0}$) and in particular medical stent devices. In Astorino et al. (2012) the same method is used to model impermeable fixed surfaces (e.g., a fully open and fully closed aortic valve), for which $\boldsymbol{R}_\Gamma = R_\Gamma \boldsymbol{I}$ with the real valued function R_Γ chosen sufficiently large to weakly enforce the fluid velocity $\boldsymbol{u}$ to be small or nearly zero in proximity of the surface Γ. In this paper, we generalize the latter case for a moving immersed surface (i.e., $\boldsymbol{u}_\Gamma \neq \boldsymbol{0}$). Furthermore, we underline that this method can be interpreted as a weak imposition of a no-slip condition on the immersed surface Γ, provided that suitable scalings with respect to the discretization parameters are introduced. For this reason, we select $\boldsymbol{R}_{\Gamma,\varepsilon} = R_\Gamma/\varepsilon\, \boldsymbol{I}$, with $\varepsilon > 0$ a suitable length scale that we will later link to the FE mesh size. In this way, we have $R_\Gamma/\varepsilon \to \infty$ for $\varepsilon \to 0$, ensuring that $\boldsymbol{u}|_\Gamma \to \boldsymbol{u}_\Gamma$.

By defining the Hilbert spaces $V = \{\boldsymbol{v} \in [H^1(\Omega)]^3 : \boldsymbol{v}|_{\partial\Omega_D} = \boldsymbol{g}\}$, $V_0 = \{\boldsymbol{v} \in [H^1(\Omega)]^3 : \boldsymbol{v}|_{\partial\Omega_D} = \boldsymbol{0}\}$, and $Q = L^2(\Omega)$ and by choosing $\boldsymbol{v} \in V_0$ and $q \in Q$ as test functions for velocity and pressure, respectively, we write the weak formulation of problem (1)–(4) as follows: find $\boldsymbol{u} \in L^2(\mathbb{R}^+; V) \cap C^0(\mathbb{R}^+; [L^2(\Omega)]^3)$ and $p \in L^2(\mathbb{R}^+; Q)$ such that, for all $\boldsymbol{v} \in V_0$ and $q \in Q$:

$$\begin{cases} \left(\rho \frac{\partial \boldsymbol{u}}{\partial t}, \boldsymbol{v}\right) + a(\boldsymbol{u}, \boldsymbol{v}) \\ \quad + c(\boldsymbol{u}, \boldsymbol{u}, \boldsymbol{v}) + b(\boldsymbol{v}, p) = F(\boldsymbol{v}) \\ -b(\boldsymbol{u}, q) = 0, \end{cases} \tag{6}$$

where we denote with $(\cdot,\cdot)$ the scalar product in $L^2(\Omega)$ and we define the following forms and linear functionals: $a : V \times V \to \mathbb{R}$, $b : V \times Q \to \mathbb{R}$, $c : V \times V \times V \to \mathbb{R}$, $F : V \to \mathbb{R}$ such that:

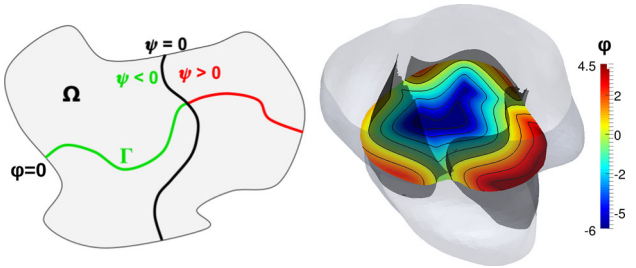

Fig. 1 The two level set functions: a 2D schematic example of the description of the immersed surface Γ through the level set functions φ and ψ (*left*); the application to the description of the aortic valve, the values of the distance function φ imaged on a slice (*right*)

$$\begin{aligned} a(\boldsymbol{u},\boldsymbol{v}) &:= \tilde{a}(\boldsymbol{u},\boldsymbol{v}) + a_\Gamma(\boldsymbol{u},\boldsymbol{v}), \\ \tilde{a}(\boldsymbol{u},\boldsymbol{v}) &:= \int_\Omega 2\mu\, \boldsymbol{D}(\boldsymbol{u}) : \boldsymbol{D}(\boldsymbol{v})\, \mathrm{d}\boldsymbol{x}, \\ a_\Gamma(\boldsymbol{u},\boldsymbol{v}) &:= \frac{R_\Gamma}{\varepsilon} \int_\Gamma (\boldsymbol{u} - \boldsymbol{u}_\Gamma)\cdot\boldsymbol{v}\, \mathrm{d}\gamma, \\ b(\boldsymbol{v},p) &:= -\int_\Omega p\nabla\cdot\boldsymbol{v}\, \mathrm{d}\boldsymbol{x}, \\ c(\boldsymbol{w},\boldsymbol{u},\boldsymbol{v}) &:= \int_\Omega \rho\big((\boldsymbol{w}\cdot\nabla)\boldsymbol{u}\big)\cdot\boldsymbol{v}\, \mathrm{d}\boldsymbol{x}, \\ F(\boldsymbol{v}) &:= \int_\Omega \boldsymbol{f}\cdot\boldsymbol{v}\, d\boldsymbol{x} + \int_{\partial\Omega_N} \boldsymbol{h}\cdot\boldsymbol{v}\, \mathrm{d}\gamma. \end{aligned} \tag{7}$$

We notice that the form $a_\Gamma(\boldsymbol{u},\boldsymbol{v})$ is associated with the definition of the "Dirac distribution" in Eq. (1), that is

$$\langle \delta_\Gamma(\boldsymbol{u} - \boldsymbol{u}_\Gamma), \boldsymbol{v}\rangle = \int_\Gamma (\boldsymbol{u} - \boldsymbol{u}_\Gamma)\cdot\boldsymbol{v}\, \mathrm{d}\gamma, \tag{8}$$

for all $\boldsymbol{v} \in V$; the method can be easily generalized to the case of N immersed surfaces Γ_i by introducing the bilinear form $a_{\Gamma,N}(\boldsymbol{u},\boldsymbol{v}) = \sum_{i=1}^N R_{\Gamma_i}/\varepsilon_i \int_{\Gamma_i} (\boldsymbol{u} - \boldsymbol{u}_{\Gamma_i})\cdot\boldsymbol{v}\, \mathrm{d}\gamma$, for some $\{\varepsilon_i\}_{i=1}^N$.

Our approach consists in describing the immersed surface Γ as an implicit surface (Osher and Fedkiw 2001). This is made by exploiting two level set functions $\varphi, \psi : \Omega \to \mathbb{R}$ and combining them to implicitly describe the open immersed surface Γ as:

$$\Gamma = \{\boldsymbol{x} \in \Omega : \varphi(\boldsymbol{x}) = 0 \text{ and } \psi(\boldsymbol{x}) \leq 0\}. \tag{9}$$

A graphical sketch of the idea is shown for a 2D case in Fig. 1, left. The use of two level set functions allows to model an open immersed surface. The first level set function φ is used to identify the immersed surface Γ as a part of its zero level; the auxiliary level set function ψ is used to cut the zero level of φ in order to obtain the final open surface Γ. Furthermore, we require that the level set function φ is a signed distance function (for which $|\nabla\varphi| = 1$). In this way, we ensure that the value of the function φ in Ω represents the signed distance

to the immersed surface Γ (Osher and Fedkiw 2001). As example, we show in Fig. 1, right, the values taken by the distance function φ at a constant level of the coordinate z, where Ω represents the aortic root and Γ is the open aortic valve.

Now, we use the two level set functions φ and ψ to describe the immersed surface Γ implicitly. First, we define a smooth Dirac function to approximate the "Dirac distribution" δ_Γ as follows:

$$\delta_\varepsilon(\varphi) = \begin{cases} \big(1+\cos\pi\varphi/\varepsilon\big)/2\varepsilon & \text{if } |\varphi| \le \varepsilon, \\ 0 & \text{if } |\varphi| > \varepsilon. \end{cases} \tag{10}$$

In this manner, we have $\int_{-\infty}^{+\infty} \delta_\varepsilon(\varphi)\, d\varphi \equiv \int_{-\varepsilon}^{+\varepsilon} \delta_\varepsilon(\varphi)\, d\varphi = 1$. We observe that the smoothing parameter ε is the same length scale of Eqs. (1) and (7) used to weakly enforce the velocity $\boldsymbol{u}$ to adhere to $\boldsymbol{u}_\Gamma$ on Γ through the resistive approach. We obtain:

$$|\Gamma| = \int_\Omega \delta_\Gamma \,\mathrm{d}\boldsymbol{x} = \int_\Omega \big(1-\mathcal{H}(\psi)\big)\,\delta_\varepsilon(\varphi)\,\mathrm{d}\boldsymbol{x}, \tag{11}$$

where $\mathcal{H}$ is the Heaviside function:

$$\mathcal{H}(\varphi) = \begin{cases} 1 & \text{if } |\varphi| \ge 0, \\ 0 & \text{if } |\varphi| < 0, \end{cases} \tag{12}$$

with the definition of Γ in Eq. (9) and the fact that φ is a signed distance function. Therefore, we approximate the resistive term $a_\Gamma(\boldsymbol{u},\boldsymbol{v})$ of Eq. (7) as:

$$\frac{R_\Gamma}{\varepsilon}\int_\Gamma (\boldsymbol{u}-\boldsymbol{u}_\Gamma)\cdot \mathrm{d}\gamma \simeq \frac{R_\Gamma}{\varepsilon}\int_\Omega \big(1-\mathcal{H}(\psi)\big)\,\delta_\varepsilon(\varphi)\,(\boldsymbol{u}-\boldsymbol{u}_\Gamma)\cdot\boldsymbol{v}\,\mathrm{d}\boldsymbol{x}, \tag{13}$$

the latter term being an approximation of $\frac{R_\Gamma}{\varepsilon}\langle\delta_\Gamma(\boldsymbol{u}-\boldsymbol{u}_\Gamma),\boldsymbol{v}\rangle$. This approximation allows to replace the surface integral on Γ with an integral in the whole domain Ω. We remark that such approximation improves for $\varepsilon \to 0$. According to this approach, one can describe a moving immersed surface by suitably defining the level set functions φ and ψ as dependent on the time variable t other than the spatial variable $\boldsymbol{x}$. These features can be introduced in virtue of the implicit definition of the immersed surface Γ and, for this reason, we name our approach resistive immersed implicit surface (RIIS). More explicitly, we redefine the bilinear form $a(\boldsymbol{u},\boldsymbol{v})$ in Eq. (7) introducing the bilinear form $a_{\mathrm{RIIS}}(\boldsymbol{u},\boldsymbol{v})$ as:

$$\begin{aligned} a(\boldsymbol{u},\boldsymbol{v}) &:= \tilde{a}(\boldsymbol{u},\boldsymbol{v}) + a_{\mathrm{RIIS}}(\boldsymbol{u},\boldsymbol{v}), \\ a_{\mathrm{RIIS}}(\boldsymbol{u},\boldsymbol{v}) &:= \frac{R_\Gamma}{\varepsilon}\int_\Omega \big(1-\mathcal{H}(\psi)\big)\delta_\varepsilon(\varphi)\,(\boldsymbol{u}-\boldsymbol{u}_\Gamma)\cdot\boldsymbol{v}\,\mathrm{d}\boldsymbol{x}. \end{aligned} \tag{14}$$

2.2 The RIIS model for the aortic valve (AV-RIIS)

We use the RIIS model to describe the blood flow through the aortic valve. For this reason, we identify the domain Ω with the anatomic region composed by the final part of the left ventricle, the aortic root, and the ascending aorta. Hence, we split the boundary as: $\partial\Omega = \partial\Omega_{\mathrm{wall}} \cup \partial\Omega_{\mathrm{in}} \cup \partial\Omega_{\mathrm{out}}$, where the three subsets of $\partial\Omega$ represent the lumen surface of the aorta, the inlet boundary in the left ventricle, and the outlet boundary at the upper end of the ascending aorta, respectively. In particular, we assume the inlet $\partial\Omega_{\mathrm{in}}$ and the outlet $\partial\Omega_{\mathrm{out}}$ boundaries as the planar surfaces orthogonal to the centerline of the vessel, with outward normals $\boldsymbol{n}_{\mathrm{in}}$ and $\boldsymbol{n}_{\mathrm{out}}$, respectively. By recalling the notation of Eq. (4) $\partial\Omega_{\mathrm{wall}} = \partial\Omega_D$ and $\partial\Omega_{\mathrm{in}} \cup \partial\Omega_{\mathrm{out}} = \partial\Omega_N$, we assign an homogeneous Dirichlet condition on $\partial\Omega_{\mathrm{wall}}$ for the velocity and Neumann conditions both on the inlet and the outlet boundaries to set the pressure:

$$\begin{aligned} \boldsymbol{u} &= \boldsymbol{0} && \text{on } \partial\Omega_{\mathrm{wall}} \times (0,T), \\ \boldsymbol{\sigma}\,\boldsymbol{n}_{\mathrm{in}} &= p_{\mathrm{in}}\,\boldsymbol{n}_{\mathrm{in}} && \text{on } \partial\Omega_{\mathrm{in}} \times (0,T), \\ \boldsymbol{\sigma}\,\boldsymbol{n}_{\mathrm{out}} &= p_{\mathrm{out}}\,\boldsymbol{n}_{\mathrm{out}} && \text{on } \partial\Omega_{\mathrm{out}} \times (0,T), \end{aligned} \tag{15}$$

where $p_{\mathrm{in}} = p_{\mathrm{in}}(t)$ and $p_{\mathrm{out}} = p_{\mathrm{out}}(t)$ are the pressure functions prescribed according to physiological values.

We define the two level set functions φ and ψ in order to represent the aortic valve at each time $t \in (0,T)$. More in detail, through the level set functions $\varphi_{\mathrm{op}}, \varphi_{\mathrm{cl}}, \psi_{\mathrm{op}}, \psi_{\mathrm{cl}} : \Omega \to \mathbb{R}$, we represent the valve in the fully open (op) and closed (cl) configurations; such functions are fixed in Ω and independent of time. Indeed, the valve remains in one of these two configurations for almost the whole cardiac cycle, except during its fast opening and closing stages. Moreover, we can reconstruct these two configurations directly from medical images in a patient-specific geometry (as will be outlined in Sect. 4), while it is basically impossible to recover the level set functions for the intermediate valve configurations (during the opening and closing stages). The configuration of the valve at each time is then obtained by linearly interpolating the open and the closed ones as:

$$\begin{aligned} \widetilde{\varphi}(\boldsymbol{x},t) &= \varphi(\boldsymbol{x},\mathcal{K}(t)) \\ &= \mathcal{K}(t)\,\varphi_{\mathrm{op}}(\boldsymbol{x}) + (1-\mathcal{K}(t))\,\varphi_{\mathrm{cl}}(\boldsymbol{x}), \\ \widetilde{\psi}(\boldsymbol{x},t) &= \psi(\boldsymbol{x},\mathcal{K}(t)) \\ &= \mathcal{K}(t)\,\psi_{\mathrm{op}}(\boldsymbol{x}) + (1-\mathcal{K}(t))\,\psi_{\mathrm{cl}}(\boldsymbol{x}), \end{aligned} \tag{16}$$

by means of a suitable time dependent *interpolation function* $\mathcal{K} : \mathbb{R} \to [0,1]$, for all t, that will be characterized later. Hence, the evolution in time of the two level set functions φ and ψ depends only on the evolution in time of the function $\mathcal{K}$. Note that the two distance functions φ_{op} and φ_{cl} must use the same sign convention, i.e., negative values within the

aortic valve (where the blood flows from the ventricle to the aortic root) and positive outside of it.

Now, we define the velocity of the aortic valve $\boldsymbol{u}_\Gamma$. We observe that the movement between its closed and its open position is mainly orthogonal to the valve surface Γ. Thus, we assume the velocity of the valve $\boldsymbol{u}_\Gamma$ to have the same direction of the normal to the surface of the valve represented by φ. Therefore, by exploiting the properties of the level set functions (Osher and Fedkiw 2001) and the fact that φ is also a signed distance function ($|\nabla\varphi| = 1$), we define the velocity of the valve as:

$$\begin{aligned}\widetilde{\boldsymbol{u}}_\Gamma(\boldsymbol{x},t) &= -\frac{\partial\widetilde{\varphi}(\boldsymbol{x},t)}{\partial t}\nabla\widetilde{\varphi}(\boldsymbol{x},t)\\ &= -\frac{\partial\varphi(\boldsymbol{x},\mathcal{K})}{\partial\mathcal{K}}\frac{d\mathcal{K}(t)}{dt}\nabla\varphi(\boldsymbol{x},\mathcal{K}(t)).\end{aligned} \tag{17}$$

Indeed, the vector $\nabla\widetilde{\varphi}$ is equivalent to the normal of the surface $\boldsymbol{n}_\Gamma$ (positive outside the aortic valve, coherently with the sign convention), while the scalar function $-\partial\widetilde{\varphi}/\partial t$ is related to the magnitude of the velocity field $\widetilde{\boldsymbol{u}}_\Gamma$ (Osher and Fedkiw 2001) since we assumed $\boldsymbol{u}_\Gamma = (\boldsymbol{u}_\Gamma\cdot\boldsymbol{n}_\Gamma)\boldsymbol{n}_\Gamma$. We notice that if the valve is opening, $-\partial\widetilde{\varphi}/\partial t$ is positive and the velocity $\widetilde{\boldsymbol{u}}_\Gamma$ takes the same direction and verse of the surface normal $\boldsymbol{n}_\Gamma$; on the contrary, if the valve is closing the quantity $-\partial\widetilde{\varphi}/\partial t$ is negative and the velocity $\widetilde{\boldsymbol{u}}_\Gamma$ takes the opposite verse of the surface normal $\boldsymbol{n}_\Gamma$. Finally, by using the definition (16) of the distance function φ, we express $\boldsymbol{u}_\Gamma$ through the function $\mathcal{K}(t)$ as:

$$\begin{aligned}\boldsymbol{u}_\Gamma(\boldsymbol{x},\mathcal{K}(t)) = \frac{d\mathcal{K}(t)}{dt}&\big(\varphi_{\mathrm{cl}}(\boldsymbol{x})-\varphi_{\mathrm{op}}(\boldsymbol{x})\big)\\ &\cdot\big(\mathcal{K}(t)\nabla\varphi_{\mathrm{op}}(\boldsymbol{x})+(1-\mathcal{K}(t))\nabla\varphi_{\mathrm{cl}}(\boldsymbol{x})\big).\end{aligned} \tag{18}$$

Equations (15), (16), and (18) determine our approach to apply the general RIIS model to the aortic valve (AV-RIIS). In summary, we describe explicitly the aortic valve in the open and closed configurations through φ_{op} and φ_{cl}, while we obtain the intermediate configurations and the valve velocity $\boldsymbol{u}_\Gamma$ through the choice of a suitable function $\mathcal{K}(t)$; we outline our approach to determine $\mathcal{K}(t)$ in Sect. 2.4.

2.3 The OD model for the aortic valve angle (AV-0D)

We exploit the 0D model proposed by Korakianitis and Shi (2006) for the aortic valve (AV-0D model) to model in a realistic way its behavior during the cardiac cycle. The AV-0D model consists in a ODE with the opening angle $\vartheta(t)$ of the valve as dependent variable, for which the forces acting on the valve are modeled by using the pressure in the left ventricle P_{lv}, the pressure in the first section of the ascending aorta P_{ao}, and the flow rate in the ascending aorta Q_{ao} as:

Table 1 Parameters of the AV-OD model for the aortic valve angle from Korakianitis and Shi (2006)

k_p ($\frac{\mathrm{rad}}{\mathrm{s}^2}$ mmHg)	k_f (s^{-1})	k_b ($\frac{rad}{s\,m}$)	k_v ($\frac{rad}{s\,m}$)	ϑ_{min}	ϑ_{max}
5500	50	2	7	5°	75°

$$\begin{cases}\frac{d^2\vartheta(t)}{dt^2}+k_f\frac{d\vartheta(t)}{dt} = k_p\left(P_{\mathrm{lv}}(t)-P_{\mathrm{ao}}(t)\right)\cos\left(\vartheta(t)\right)\\ \quad -k_v\ \mathrm{sgn}(Q_{\mathrm{ao}}(t))\,Q_{\mathrm{ao}}(t)\,\sin\left(2\vartheta(t)\right)\\ \quad +k_b\,Q_{\mathrm{ao}}(t)\,\cos\left(\vartheta(t)\right)\qquad \forall t\in(0,T),\\ \vartheta(0)=\vartheta_{\min},\\ \frac{d\vartheta(0)}{dt}=0,\end{cases} \tag{19}$$

where $\mathrm{sgn}(\cdot)$ is the sign function; k_f, k_p, k_v, and k_b are suitable valve parameters. Since the aortic valve yields a fixed angle when totally open or closed, the model also defines minimum $\vartheta_{\min}$ and maximum $\vartheta_{\max}$ angles leading to the constraint $\vartheta(t)\in[\vartheta_{\min},\vartheta_{\max}]$, for all t. The values of the parameters originally proposed in (Korakianitis and Shi 2006) for a physiological aortic valve are shown in Table 1.

2.4 Coupling the AV-0D and the AV-RIIS models

We now couple the (3D) AV-RIIS fluid dynamics model with the AV-0D valve model. First, we define the relations between the pressure values P_{lv} and P_{ao} and the flow rate Q_{ao} involved in the AV-0D model (19) and the pressure p and the velocity $\boldsymbol{u}$ in the AV-RIIS 3D model as:

$$\begin{aligned}P_{\mathrm{lv}}(t) &= |\Omega_{\mathrm{lv}}|^{-1}\int_{\Omega_{\mathrm{lv}}}p(\boldsymbol{x},t)\,\mathrm{d}\boldsymbol{x},\\ P_{\mathrm{ao}}(t) &= |\Omega_{\mathrm{ao}}|^{-1}\int_{\Omega_{\mathrm{ao}}}p(\boldsymbol{x},t)\,\mathrm{d}\boldsymbol{x},\\ Q_{\mathrm{ao}}(t) &= -\int_{\partial\Omega_{\mathrm{in}}}\boldsymbol{u}(\boldsymbol{x},t)\cdot\boldsymbol{n}_{\mathrm{in}}(\boldsymbol{x})\,\mathrm{d}\gamma,\end{aligned} \tag{20}$$

where Ω_{lv} and Ω_{ao} are two suitable control volumes taken upstream the aortic valve (i.e., in the proximity of the left ventricle base) and downstream (at the initial section of the ascending aorta), respectively.

We now link the AV-RIIS model to the AV-0D model through the interpolation function $\mathcal{K}(t)$ of Eq. (16). For this reason, we introduce the concept of the valvular plane Γ_{vp}, a fixed plane parallel to the annulus (Charitos and Sievers 2013) used in radiology to track the dynamics of the valve and of its orifice. Also, we introduce the characteristic function $\chi_{\{\boldsymbol{x}:\varphi(\boldsymbol{x},\mathcal{K})<0\}}$ to select only the set of points where the distance function φ of Eq. (16) is negative, i.e., the region within the aortic valve:

$$\chi_{\{\boldsymbol{x}:\varphi(\boldsymbol{x},\mathcal{K})<0\}}(\boldsymbol{x}) = \begin{cases} 1 & \text{if } \varphi(\boldsymbol{x},\mathcal{K}) < 0, \\ 0 & \text{if } \varphi(\boldsymbol{x},\mathcal{K}) \geq 0. \end{cases} \tag{21}$$

By exploiting both the valvular plane Γ_{vp} and the characteristic function $\chi_{\{\boldsymbol{x}:\varphi(\boldsymbol{x},\mathcal{K})<0\}}$, we can define the Orifice Area (OA) as a function of $\mathcal{K}$:

$$\mathrm{OA}(\mathcal{K}) = \int_{\Gamma_{\mathrm{vp}}} \chi_{\{\boldsymbol{x}:\varphi(\boldsymbol{x},\mathcal{K})<0\}}(\boldsymbol{x})\,\mathrm{d}\gamma. \tag{22}$$

The maximum orifice area $\mathrm{OA}_{\max}$, corresponding to the fully open valve, is obtained by setting $\mathcal{K} = 1$ in the above definition:

$$\mathrm{OA}_{\max} = \int_{\Gamma_{vp}} \chi_{\{\boldsymbol{x}:\varphi(\boldsymbol{x},1)<0\}}(\boldsymbol{x})\,\mathrm{d}\gamma. \tag{23}$$

Korakianitis and Shi (2006) introduced the area resistance ($\mathrm{AR}_{\mathrm{ao}}$) coefficient representing the resistance to the blood flow through the orifice; in this AV-0D model, $\mathrm{AR}_{\mathrm{ao}}$ is dependent on the opening angle ϑ as:

$$\mathrm{AR}_{\mathrm{ao}}(\vartheta) = \frac{\big(1-\cos(\vartheta)\big)^2}{\big(1-\cos(\vartheta_{\max})\big)^2}. \tag{24}$$

We define the coefficient $\widetilde{\mathrm{AR}}_{\mathrm{ao}}$ as the opening fraction of the valvular orifice in terms of $\mathcal{K}$ as:

$$\widetilde{\mathrm{AR}}_{\mathrm{ao}}(\mathcal{K}) := \frac{\mathrm{OA}\big(\mathcal{K}\big)}{\mathrm{OA}_{\max}}. \tag{25}$$

Then, we find $\mathcal{K}$ such that: $\widetilde{\mathrm{AR}}_{\mathrm{ao}}(\mathcal{K}) \equiv \mathrm{AR}_{\mathrm{ao}}(\vartheta)$ for any given ϑ; this corresponds to reinterpret the resistance to the blood flow introduced by Korakianitis and Shi (2006) as the fraction of opening of the valvular orifice. Since $\widetilde{\mathrm{AR}}_{\mathrm{ao}}$ depends only on the function $\mathcal{K}$, enforcing $\widetilde{\mathrm{AR}}_{\mathrm{ao}}(\mathcal{K}) \equiv \mathrm{AR}_{\mathrm{ao}}(\vartheta)$ couples the AV-0D and the AV-RIIS models; more explicitly, we have the following nonlinear coupling equation:

$$\mathrm{OA}(\mathcal{K}(t)) - \mathrm{AR}_{\mathrm{ao}}(\vartheta(t))\,\mathrm{OA}_{\max} = 0 \quad \forall t \in (0,T). \tag{26}$$

2.5 The reduced 3D–0D FSI model

We write now the fully coupled reduced 3D-0D FSI model: for all $t \in (0,T)$, find $\boldsymbol{u} : \Omega \to \mathbb{R}^3$, $p : \Omega \to \mathbb{R}$, $\vartheta \in [\vartheta_{\min}, \vartheta_{\max}]$, and $\mathcal{K} \in [0,1]$ such that, for all $\boldsymbol{v} \in V_0$ and $q \in Q$:

$$\begin{aligned}
&\textbf{AV-RIIS} \begin{cases} \big(\rho \tfrac{\partial \boldsymbol{u}}{\partial t}, \boldsymbol{v}\big) + \bar{a}(\boldsymbol{u},\boldsymbol{v},\mathcal{K}) \\ \quad + c(\boldsymbol{u},\boldsymbol{u},\boldsymbol{v}) + b(\boldsymbol{v},p) = F(\boldsymbol{v}) - b(\boldsymbol{u},q) = 0 \end{cases} \\
&\textbf{AV-0D} \begin{cases} \frac{d^2\vartheta}{dt^2} + k_f \frac{d\vartheta}{dt} = k_p\,(P_{\mathrm{lv}} - P_{\mathrm{ao}})\cos(\vartheta) \\ \quad - k_v\ \mathrm{sgn}(Q_{\mathrm{ao}})\,Q_{\mathrm{ao}}\ \sin(2\vartheta) \\ \quad + k_b\,Q_{\mathrm{ao}}\ \cos(\vartheta) \end{cases} \\
&\textbf{coupling}\ \{ OA(\mathcal{K}) - AR_{\mathrm{ao}}(\vartheta)\,OA_{\max} = 0,
\end{aligned} \tag{27}$$

with initial conditions $\boldsymbol{u}(\boldsymbol{x},0) = \boldsymbol{0}$, $\vartheta(0) = \vartheta_{\min}$, and $\mathrm{d}\vartheta/\mathrm{d}t(0) = 0$ (for which also $\mathcal{K}(0) \equiv 0$), where:

$$\begin{aligned}
\bar{a}(\boldsymbol{u},\boldsymbol{v},\mathcal{K}) &:= \tilde{a}(\boldsymbol{u},\boldsymbol{v}) + \bar{a}_{\mathrm{RIIS}}(\boldsymbol{u},\boldsymbol{v},\mathcal{K}), \\
\tilde{a}(\boldsymbol{u},\boldsymbol{v}) &= 2\mu \int_\Omega \boldsymbol{D}(\boldsymbol{u}) : \boldsymbol{D}(\boldsymbol{v})\,\mathrm{d}\boldsymbol{x}, \\
\bar{a}_{\mathrm{RIIS}}(\boldsymbol{u},\boldsymbol{v},\mathcal{K}) &= \frac{R_\Gamma}{\varepsilon} \int_\Omega \big(1 - \mathcal{H}(\psi(\mathcal{K}))\big) \\
&\qquad \cdot \delta_\varepsilon(\varphi(\mathcal{K}))(\boldsymbol{u} - \boldsymbol{u}_\Gamma)\cdot\boldsymbol{v}\,\mathrm{d}\boldsymbol{x}, \\
\varphi(\mathcal{K}) &= \mathcal{K}\,\varphi_{\mathrm{op}} + (1-\mathcal{K})\,\varphi_{\mathrm{cl}}, \\
\psi(\mathcal{K}) &= \mathcal{K}\,\psi_{\mathrm{op}} + (1-\mathcal{K})\,\psi_{\mathrm{cl}}, \\
\boldsymbol{u}_\Gamma(\mathcal{K}) &= \frac{\mathrm{d}\mathcal{K}}{\mathrm{d}t}\big(\varphi_{\mathrm{cl}} - \varphi_{\mathrm{op}}\big) \\
&\qquad \cdot \big(\mathcal{K}\nabla\varphi_{\mathrm{op}} + (1-\mathcal{K})\nabla\varphi_{\mathrm{cl}}\big), \\
b(\boldsymbol{v},p) &= -\int_\Omega p\nabla\cdot\boldsymbol{v}\,\mathrm{d}\boldsymbol{x}, \\
c(\boldsymbol{w},\boldsymbol{u},\boldsymbol{v}) &= \rho\int_\Omega \big((\boldsymbol{w}\cdot\nabla)\boldsymbol{u}\big)\cdot\boldsymbol{v}\,\mathrm{d}\boldsymbol{x}, \\
F(\boldsymbol{v}) &= \int_{\partial\Omega_{\mathrm{in}}} p_{\mathrm{in}}\boldsymbol{n}_{\mathrm{in}}\cdot\boldsymbol{v}\,\mathrm{d}\gamma \\
&\qquad + \int_{\partial\Omega_{\mathrm{out}}} p_{\mathrm{out}}\boldsymbol{n}_{\mathrm{out}}\cdot\boldsymbol{v}\,\mathrm{d}\gamma, \\
P_{\mathrm{lv}} &= |\Omega_{\mathrm{lv}}|^{-1}\int_{\Omega_{\mathrm{lv}}} p\,\mathrm{d}\boldsymbol{x}, \\
P_{\mathrm{ao}} &= |\Omega_{\mathrm{ao}}|^{-1}\int_{\Omega_{\mathrm{ao}}} p\,\mathrm{d}\boldsymbol{x}, \\
Q_{\mathrm{ao}} &= -\int_{\partial\Omega_{\mathrm{in}}} \boldsymbol{u}\cdot\boldsymbol{n}_{\mathrm{in}}\,\mathrm{d}\gamma, \\
\mathrm{OA}(\mathcal{K}) &= \int_{\Gamma_{\mathrm{vp}}} \chi_{\{\boldsymbol{x}:\varphi(\boldsymbol{x},\mathcal{K})<0\}}\,\mathrm{d}\gamma, \\
\mathrm{AR}_{\mathrm{ao}}(\vartheta) &= \frac{\big(1-\cos(\vartheta)\big)^2}{\big(1-\cos(\vartheta_{\max})\big)^2}.
\end{aligned} \tag{28}$$

The coupled problem of Eq. (27) represents a reduced 3D–0D FSI model; indeed the 3D fluid equations are coupled with a simple 0D model for the valve; the latter condensates the mechanical properties of the valve and its dynamics onto a single kinematic variable, i.e., the "averaged" opening angle ϑ.

3 Numerical approximation

We focus on the numerical approximation of the fully coupled model (27). First, we discretize the three submodels of the problem (27) separately.

3.1 AV-RIIS model: space and time discretizations

The AV-RIIS model of Eq. (27) is discretized in space using the stabilized FE method (Quarteroni 2014) for which the approximated velocity and pressure variables are built from Lagrangian polynomial basis functions of equal degree. More formally, let $\mathcal{T}_h$ be a tetrahedralization of our domain $\Omega \subset \mathbb{R}^3$ representing the aortic root such that $\Omega = \bigcup_{T\in\mathcal{T}_h} T$ and $h = \max_{T\in\mathcal{T}_h}(\mathrm{diam}(T))$. We introduce the space:

$$X_h^r = \left\{ v_h \in C^0(\bar{\Omega}) : v_h|_T \in \mathbb{P}^r, \quad r \geq 1, \quad \forall T \in \mathcal{T}_h \right\}, \tag{29}$$

where we denote with $\mathbb{P}^r$ the finite dimensional space of polynomials of degree r. We define the FE spaces for the velocity as $V_h^r = ([X_h^r]^3 \cap V_0)$ and for the pressure as $Q_h^r = X_h^r \cap Q$.

We consider the time discretization by means of backward differentiation formula (BDF) of a generic order $\sigma = 1, 2, \ldots$ and by adopting a semi-implicit treatment for the nonlinear term, through equal order extrapolation (Gauthier et al. 2004). In order to limit the computational burden of the spatial discretization we choose equal order FE spaces V_h^r and Q_h^r, which are not inf-sup stable and require a suitable stabilization. In order to obtain a stable formulation and to control numerical instabilities associated with the highly advective flow regime in the valve, we consider and extend to the AV-RIIS case the streamline upwind Petrov–Galerkin (SUPG) stabilization for the Navier–Stokes equations. Furthermore, as proposed by Forti and Dedè (2015) for time discretization based on the BDF scheme, we set the SUPG parameters in a straightforward way following the variational multiscale (VMS) concept (Bazilevs et al. 2007). More in details, after partitioning the time interval $(0, T)$ into time instants $\{t_n\}_{n=0}^N$ equally spaced by Δt, we stabilize both the momentum and the continuity equation as follows: for all $n \geq \sigma$, assuming that $\mathcal{K}^n$ and $\boldsymbol{u}_h^{n-i}$ for $i = 1, \ldots, \sigma$ are given, we find $\boldsymbol{u}_h^n \in V_h^r$ and $p_h^n \in Q_h^r$ such that:

$$\begin{aligned}
&\left(\rho\frac{\alpha_\sigma \boldsymbol{u}_h^n - \boldsymbol{u}_h^{n,\mathrm{BDF}\sigma}}{\Delta t}, \boldsymbol{v}_h\right) + \bar{a}(\boldsymbol{u}_h^n, \boldsymbol{v}_h, \mathcal{K}^n) \\
&\quad + c\left(\boldsymbol{u}_h^{n,\sigma}, \boldsymbol{u}_h^n, \boldsymbol{v}_h\right) + b\left(\boldsymbol{v}_h, p_h^n\right) - b\left(\boldsymbol{u}_h^n, q_h\right) \\
&\quad + \left(\tau_M^{n,\sigma}\boldsymbol{r}_M^n\left(\boldsymbol{u}_h^n, p_h^n\right), \rho\left(\boldsymbol{u}_h^{n,\sigma}\cdot\nabla\right)\boldsymbol{v}_h + \nabla q_h\right) \\
&\quad - \left(\tau_C^{n,\sigma} r_C^n\left(\boldsymbol{u}_h^n\right), \nabla\cdot\boldsymbol{v}_h\right) = F(\boldsymbol{v}_h)
\end{aligned} \tag{30}$$

for all $\boldsymbol{v}_h \in V_h^r$ and $q_h \in Q_h^r$, where $\bar{a}(\cdot,\cdot)$, $b(\cdot,\cdot)$, $c(\cdot,\cdot,\cdot)$, $F(\cdot)$ are defined in Eq. (28) and α_σ, $\boldsymbol{u}_h^{n,\mathrm{BDF}\sigma}$, and the extrapolated velocity $\boldsymbol{u}_h^{n,\sigma}$ depend on the order σ of the BDF scheme; see (Forti and Dedè 2015). The two terms $\boldsymbol{r}_M^n$ and r_C^n represent the residuals of the momentum and continuity equations, the former including the RIIS term:

$$\begin{aligned}
\boldsymbol{r}_M^n(\boldsymbol{u}_h^n, p_h^n) &= \rho\frac{\alpha_\sigma\boldsymbol{u}_h^n - \boldsymbol{u}_h^{n,\mathrm{BDF}\sigma}}{\Delta t} - \mu\Delta\boldsymbol{u}_h^n \\
&\quad + \rho\left(\boldsymbol{u}_h^{n,\sigma}\cdot\nabla\right)\boldsymbol{u}_h^n + \nabla p_h^n \\
&\quad + \frac{R_\Gamma}{\varepsilon}\left(1 - \mathcal{H}(\psi(\mathcal{K}^n))\right)\delta_\varepsilon(\varphi(\mathcal{K}^n))\left(\boldsymbol{u}_h^n - \boldsymbol{u}_\Gamma^n\right), \\
r_C^n(\boldsymbol{u}_h^n) &= \nabla\cdot\boldsymbol{u}_h^n,
\end{aligned} \tag{31}$$

while $\tau_M^{n,\sigma}$ and $\tau_C^{n,\sigma}$ are the stabilization parameters, set as:

$$\begin{aligned}
\tau_M^{n,\sigma} &= \left(\frac{4\rho^2}{\Delta t^2} + \frac{\rho^2}{h^2}\left|\boldsymbol{u}_h^{n,\sigma}\right|^2 + C_r\frac{\mu^2}{h^4}\right. \\
&\quad \left. + \frac{R_\Gamma^2}{\varepsilon^2}\left(1 - \mathcal{H}(\psi(\mathcal{K}^n))\right)^2\delta_\varepsilon^2(\varphi(\mathcal{K}^n))\right)^{-\frac{1}{2}}, \\
\tau_C^{n,\sigma} &= \frac{h^2}{\tau_M^{n,\sigma}},
\end{aligned} \tag{32}$$

where $C_r = 60 \times 2^{r-2}$. We remark that, as in Forti and Dedè (2015), we extrapolate both the residual and the stabilization parameters in time according to the BDF scheme. The stabilization parameters (32) strictly depend on the local spatial discretization h and on the local velocity magnitude (Forti and Dedè 2015). Moreover, in our approach, $\tau_M^{n,\sigma}$ and $\tau_C^{n,\sigma}$ also depend on the resistive term and its location in Ω through Γ; the choice of $\tau_M^{n,\sigma}$ is motivated by the presence of the RIIS term in the momentum equation of the Navier–Stokes equations. Concerning the RIIS term in $\bar{a}(\boldsymbol{u}_h^n, \boldsymbol{v}_h, \mathcal{K}^n)$, we evaluate the two level set functions φ and ψ at the current time using $\mathcal{K}^n$ and, coherently, we use a BDF scheme to discretize the time derivative of $\mathcal{K}$, as:

$$\begin{aligned}
\bar{a}_{\mathrm{RIIS}}(\boldsymbol{u}_h^n, \boldsymbol{v}_h, \mathcal{K}^n) &= \frac{R_\Gamma}{\varepsilon}\int_\Omega \left(1 - \mathcal{H}(\psi(\mathcal{K}^n))\right) \\
&\quad \cdot \delta_\varepsilon(\varphi(\mathcal{K}^n))\left(\boldsymbol{u}_h^n - \boldsymbol{u}_\Gamma^{n,\sigma}\right)\cdot\boldsymbol{v}_h\, d\boldsymbol{x}, \\
\boldsymbol{u}_\Gamma^{n,\sigma} &= \frac{\alpha^\sigma\mathcal{K}^n - \mathcal{K}^{n,BDF\sigma}}{\Delta t}\left(\varphi_{\mathrm{cl}} - \varphi_{\mathrm{op}}\right) \\
&\quad \cdot\left(\mathcal{K}^n\nabla\varphi_{\mathrm{op}} + (1 - \mathcal{K}^n)\nabla\varphi_{\mathrm{cl}}\right).
\end{aligned} \tag{33}$$

We remark that the level set functions φ_{cl}, φ_{op}, ψ_{cl}, and ψ_{op} are not discretized in space, since we define them analytically (as described in Sect. 4); hence, these can be evaluated directly at the quadrature nodes. Even if the described method can be solved with an arbitrary order $r \geq 1$ of the FE spaces and an arbitrary order $\sigma \geq 1$ of the BDF scheme, we adopt

linear polynomials for the spatial approximation ($r = 1$) and a second-order scheme (BDF2, $\sigma = 2$) for the time approximation for which:

$$\begin{aligned} \alpha_\sigma &= \tfrac{3}{2}, \\ \boldsymbol{u}_h^{n,\mathrm{BDF}\sigma} &= 2\boldsymbol{u}_h^{n-1} - \tfrac{1}{2}\boldsymbol{u}_h^{n-2}, \\ \boldsymbol{u}_h^{n,\sigma} &= 2\boldsymbol{u}_h^{n-1} - \boldsymbol{u}_h^{n-2}, \\ \mathcal{K}^{n,\mathrm{BDF}\sigma} &= 2\mathcal{K}_h^{n-1} - \tfrac{1}{2}\mathcal{K}_h^{n-2}. \end{aligned} \tag{34}$$

This spatial approximation should yield, in principle, first order accuracy in V-norm for the velocity and in Q-norm for the pressure. However, since we deal with the Navier–Stokes equations with the SUPG stabilization method, the order of accuracy of the fluid problem itself still remains an open issue, especially with the inclusion of the resistive terms in the formulation.

3.2 The reduced 3D–0D FSI model: numerical approximation

Given the initial condition $\boldsymbol{u}_h^j = \boldsymbol{0}$ and $\vartheta^j = \vartheta_{\min}$ ($\mathcal{K}^j = 0$), for $j = 0, \ldots, \sigma - 1$, the numerical solution of the full system (27) consists in a staggered strategy based on the semi-implicit discretization of the AV-RIIS model and an explicit scheme for the AV-OD model: at each time instant t^n for which $n \geq \sigma$, given P_{lv}^{n-1}, P_{ao}^{n-1}, Q_{ao}^{n-1}, ϑ^{n-1}, $\boldsymbol{u}_h^{n-i}$, $\mathcal{K}^{n-i}$, $i = 1, \ldots, \sigma$, we find $\boldsymbol{u}_h^n$, p_h^n, ϑ^n and $\mathcal{K}^n$ as follows:

1. Find ϑ^n solving the AV-0D ODE in (27) with an explicit fourth-order Runge–Kutta method (Quarteroni et al. 2010), using ϑ^{n-1}, P_{lv}^{n-1}, P_{ao}^{n-1}, and Q_{ao}^{n-1};
2. Given ϑ^n, find $\mathcal{K}^n \in [0, 1]$ solving the nonlinear coupling equation (26) using the bisection method; indeed, we reinterpret the equation as the root finding of a nonlinear monotone function G in $\mathcal{K}^n$ such that $G(0)G(1) \leq 0$ for all $\vartheta^n \in [\vartheta_{\min}, \vartheta_{\max}]$, where:

$$G(\mathcal{K}^n) = \mathrm{OA}(\mathcal{K}^n) - \frac{\left(1 - \cos(\vartheta^n)\right)^2}{\left(1 - \cos(\vartheta_{\max})\right)^2}\,\mathrm{OA}_{\max}; \tag{35}$$

3. Given $\mathcal{K}^n$, find the solution of the discrete AV-RIIS model $(\boldsymbol{u}_h^n, p_h^n)$ solving the linear system stemming from the semi-implicit formulation (30);
4. Update P_{lv}^n, P_{ao}^n, and Q_{ao}^n using Eq. (20) and the computed solution $(\boldsymbol{u}_h^n, p_h^n)$ of the AV-RIIS model.

4 Patient-specific modeling: geometry and boundary conditions

In this section, we focus on the patient-specific geometry reconstruction of the aortic root and valve from medical images; first, we deal with a reference dataset and then with the description of the methods used to reconstruct the aortic root and lumen and the aortic valve leaflets. We describe our method by applying it to the reference dataset without loss of generality. Similarly, it can be applied to any other medical image provided the valve leaflets are at least partially visible in their closed and open configurations.

4.1 Patient dataset

The data that we use correspond to a patient routinely referred to the Cardiac Surgery Department of Ospedale Sacco, Milano, Italy. A Philips Brilliance CT 64-slice system is employed to perform a 3D contrast-enhanced computed tomography (3D-CE-CT) study with a slice thickness of 0.67 mm, a slice spacing of 0.33 mm, a reconstruction matrix of 512 × 512 pixels, and a final resolution of 0.45 mm × 0.45 mm × 0.33 mm. The 3D-CE-CT images were acquired by a retrospective ECG-gated protocol, and ten scan volumes were generated at different instants of the cardiac cycle. The International Review Board approval was obtained for the conduct of this study, and the board waived the need for patient consent.

4.2 Aortic lumen reconstruction

A surface model of the last part of the left ventricle, the aortic root, and the ascending aorta is obtained from the medical images previously described. In particular, we select a diastolic image from those available because this configuration is assumed for the most part of the cardiac cycle (Fig. 2, left). We use a region-based segmentation technique named connected component localization of the region-scalable fitting energy originally proposed in Fedele et al. (2015). The method is based on the minimization of the region-scalable fitting energy through the split Bregman method as proposed in Yang et al. (2010) and incorporates an iterative connected component extraction. Since the method depends on the image intensity values, we perform an image preprocessing to enhance the contrast between the aorta vessel and the background and to delete the nearby organs with similar image intensity (Fedele et al. 2015) (Fig. 2, center). We highlight that we choose this method because of its ability to automatically reconstruct in a single step and in a precise way the aortic root with the sinuses of Valsalva, the ascending aorta, and the aortic arch. The output of the method is a triangulated surface representing the interface between the vessel lumen and the arterial wall, see Fig. 2, right.

4.3 Aortic Valve Reconstruction

We describe how to reconstruct—starting from the medical images—the open and closed valves and, consequently,

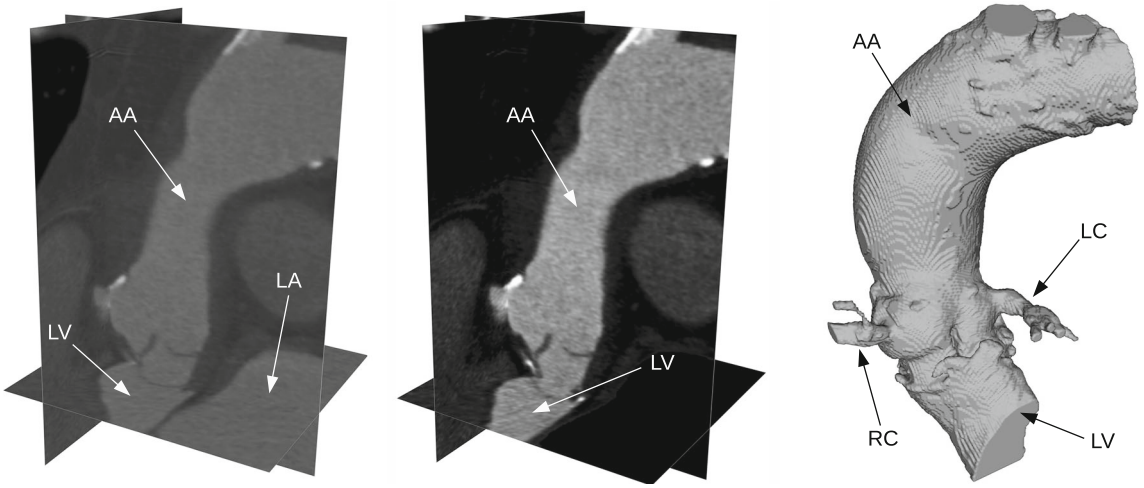

Fig. 2 Aortic lumen reconstruction: original diastolic 3D-CE-CT image cropped in proximity of the region of interest (*left*), preprocessed image (*center*) and reconstructed surface (*right*). The ascending aorta (AA), the left ventricle (LV), the left atrium (LA), and the right (RC) and left (LC) coronary arteries are indicated

how to analytically define the two pairs of level set functions $(\varphi_{\mathrm{cl}}, \psi_{\mathrm{cl}})$ and $(\varphi_{\mathrm{op}}, \psi_{\mathrm{op}})$ which represent the two valve configurations in our mathematical model. Indeed, we recall that, consistently with Eq. (9), we define the implicit surfaces representing the closed valve Γ_{cl} and the open valve Γ_{op} as:

$$\begin{aligned} \Gamma_{\mathrm{cl}} &= \{\boldsymbol{x} \in \Omega : \varphi_{\mathrm{cl}}(\boldsymbol{x}) = 0 \quad \text{and} \quad \psi_{\mathrm{cl}}(\boldsymbol{x}) \leq 0\}, \\ \Gamma_{\mathrm{op}} &= \left\{\boldsymbol{x} \in \Omega : \varphi_{\mathrm{op}}(\boldsymbol{x}) = 0 \quad \text{and} \quad \psi_{\mathrm{op}}(\boldsymbol{x}) \leq 0\right\}. \end{aligned} \tag{36}$$

The general idea of our reconstruction method consists in selecting in the diastolic and systolic images some sets of control points lying on the leaflets, and then performing a polynomial fitting on each resulting cloud of points associated with either Γ_{cl} or Γ_{op}; finally, such polynomials are combined in order to define an expression for each level set function.

As a preliminary step, we semi-automatically rotate the 3D-CE-CT reference system in order to have the z-axis growing distally and orthogonally to the valvular plane, which in radiology is referred as the plane passing through the aortic annulus (Charitos and Sievers 2013). Choosing a reference system in this way makes the valve leaflets more visible in a 3D-CE-CT image. We apply this rotation to a diastolic image (the same used for the aortic surface reconstruction) and to a systolic image in which the leaflets are completely open; concerning the systolic image, the transformation also takes into account for the misregistration between the two acquisitions which is due to the movement of the aorta and, possibly, the movement of the patient. In Fig. 3, top, we show the closed and open leaflets in a plane orthogonal to the z-axis of the new reference system (x, y, z).

The selection of control points and the polynomial fitting are performed in a different manner for the two valve configurations. In the rest of this section, we indicate with p the polynomial surfaces described as explicit functions of the z coordinate ($z = p(x, y)$) and with P the corresponding implicit descriptions ($P(\boldsymbol{x}) = P(x, y, z) = z - p(x, y)$); also, we underline the degree of the polynomial as subscript and the related leaflets as superscripts (L, R and N for the left, the right and the non-coronary leaflet, respectively).

Closed valve For each leaflet, we collect three sets of control points: in the distal part, characterized by the region of leaflet coaptation (Fig. 3, top-left), we perform two first degree polynomial fittings, each one representing two attached leaflets between two sinuses of Valsalva; instead, the proximal part, where the leaflet is clearly separated from the others (Fig. 3, top-center), is described by a second-degree polynomial. The existence of two clearly distinguishable regions in the closed leaflet is physiological, as reported for example by Charitos and Sievers (2013). As an example, in Fig. 3, mid-left, we represent for the left coronary leaflet the three clouds with different shapes of points: the triangular and squared points, where two leaflets are attached to each other, lead to the polynomials p_1^{NL} and p_1^{LR}, respectively; the cloud made of circular points leads to the second-order polynomial p_2^{L}. Consequently, we define the implicit surfaces $P_1^{\mathrm{NL}}(\boldsymbol{x})$, $P_1^{\mathrm{LR}}(\boldsymbol{x})$ and $P_2^{\mathrm{L}}(\boldsymbol{x})$.

Open valve For each open leaflet (Fig. 3, top-right), we proceed as follows: first, as shown for the left coronary leaflet in Fig. 3, mid-center, we collect a unique cloud of points and we repeat at greater z the points in the final distal part of the

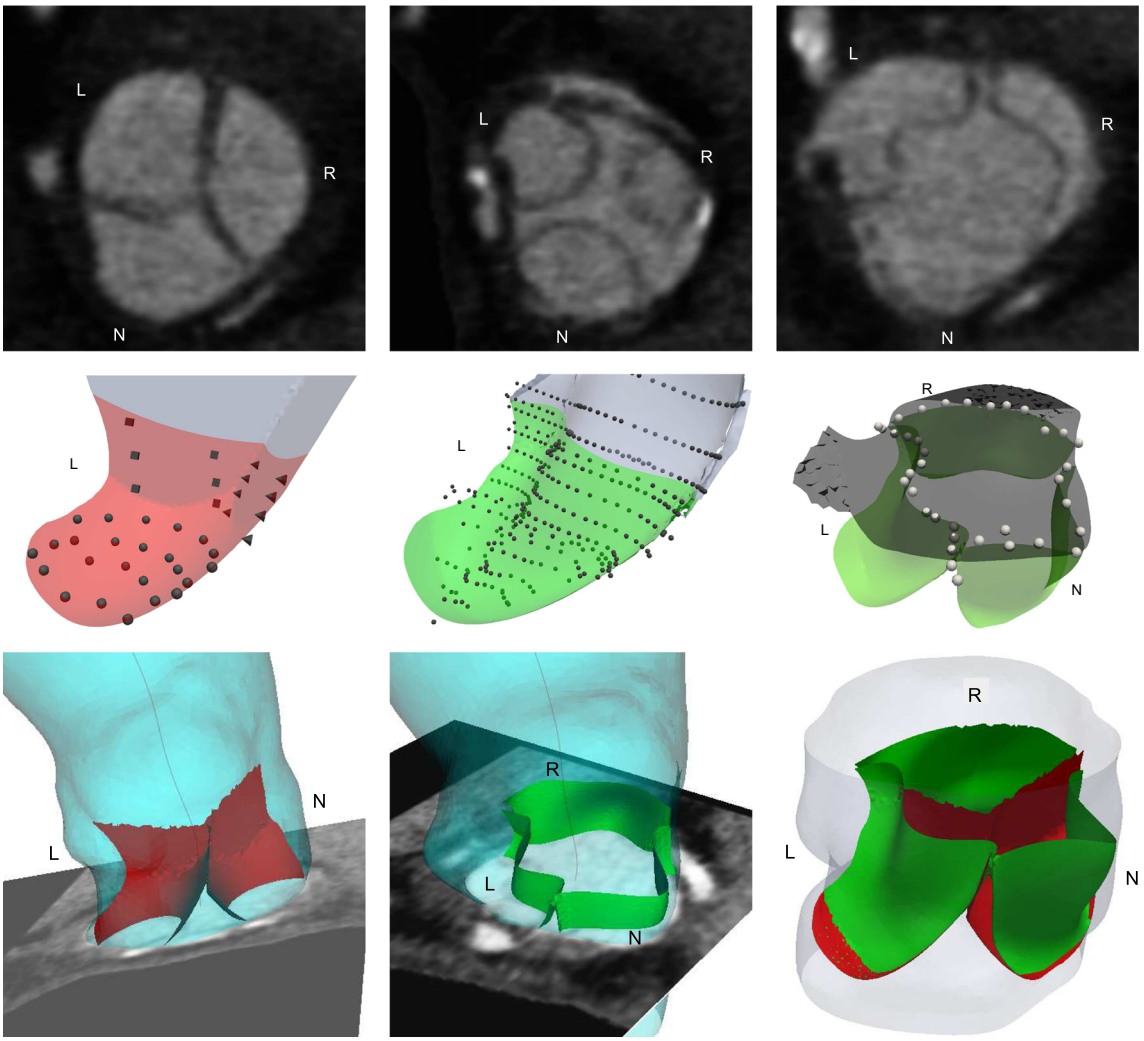

Fig. 3 View of the 3D-CE-CT medical image in planes parallel to the valvular plane (*top*): diastolic image with the distal (*top-left*) and the proximal (*top-center*) parts of the closed leaflets and systolic image with the open leaflets (*top-right*). Three examples of clouds of control points with the corresponding level set in transparency (*mid*): $\varphi_{L,\mathrm{cl}}$ (*mid-left*), $\varphi_{L,\mathrm{op}}$ (*mid-center*) and ψ_{op} (*mid-right*). The reconstructed closed (*bottom-left*) and open (*bottom-center*) leaflets superimposed to the 3D-CE-CT medical image and compared to each other (*bottom-right*). The left coronary (L), the right coronary (R) and the non-coronary (N) sinuses of Valsalva are indicated

leaflet; second, we rotate the coordinate system (x, y, z) in order to have the z-axis orthogonal to the leaflet, defining a leaflet-specific reference system; finally, we fit each set of points with an explicit fifth degree polynomial and we find the corresponding implicit description in the original reference system (x, y, z) applying the opposite rotation to the coordinates. For instance, in the case of the left coronary leaflet the rotation leads to a new reference system $(x^{\mathrm{L}}, y^{\mathrm{L}}, z^{\mathrm{L}})$ where we define the explicit polynomial $p_5^L(x^{\mathrm{L}}, y^{\mathrm{L}})$ and the corresponding implicit description $P_5^L(\boldsymbol{x}^{\mathrm{L}})$; applying the inverse rotation to the coordinates we find the desired implicit surface $P_5^L(\boldsymbol{x})$.

We now define the two level set functions φ_{op} and φ_{cl} as a combination of the implicit polynomial surfaces just defined:

1. For each leaflet, we change the sign of the implicit functions involved in its definition (e.g., P_1^{NL}, P_1^{LR}, P_2^{L}, and P_5^{L} for the left coronary leaflet) in order to yield a positive sign outside the valve orifice and a negative one otherwise;
2. For each closed leaflet, we apply the minimum operator to the three involved polynomials; e.g., for the left coronary leaflet we have:

$$\varphi_{L,\mathrm{cl}}(\boldsymbol{x}) = \min\left\{P_1^{\mathrm{NL}}(\boldsymbol{x}),\quad P_1^{\mathrm{LR}}(\boldsymbol{x}),\quad P_2^{\mathrm{L}}(\boldsymbol{x})\right\}; \quad (37)$$

3. For each open leaflet, we apply the minimum operator between the related fifth degree polynomial and the corresponding closed leaflet expression just defined; e.g., for the left coronary leaflet we have:

$$\varphi_{L,\mathrm{op}}(\boldsymbol{x}) = \min\left\{P_5^{\mathrm{L}}(\boldsymbol{x}),\quad \varphi_{L,\mathrm{cl}}(\boldsymbol{x})\right\}, \tag{38}$$

this operation further accounts for the movements of the aorta between the open and closed configurations, thus guaranteeing that the open and closed leaflets are attached at the same position in the annulus (see Fig. 3, bottom-right);

4. For each configuration, we finally define the complete level set functions φ_{op} and φ_{cl} using the maximum operator between the three leaflets expressions:

$$\begin{aligned}\varphi_{\mathrm{op}}(\boldsymbol{x}) &= \max\left\{\varphi_{N,\mathrm{op}}(\boldsymbol{x}), \varphi_{L,\mathrm{op}}(\boldsymbol{x}), \varphi_{R,\mathrm{op}}(\boldsymbol{x})\right\}\\ \varphi_{\mathrm{cl}}(\boldsymbol{x}) &= \max\left\{\varphi_{N,\mathrm{cl}}(\boldsymbol{x}), \varphi_{L,\mathrm{cl}}(\boldsymbol{x}), \varphi_{R,\mathrm{cl}}(\boldsymbol{x})\right\}.\end{aligned} \tag{39}$$

Concerning the auxiliary level set functions ψ_{cl} and ψ_{op}, for each configuration, we select a unique set of points lying on the final distal part of the leaflets (Fig. 3, mid-right) and we perform a fifth degree polynomial fitting that defines directly the two implicit expressions. Finally, as last step of the method, we perform a regularization of the level set functions φ_{cl} and φ_{op} in order to ensure that these are signed distance functions (Osher and Fedkiw 2001) (the regularized function φ_{op} is previously shown in Fig. 1, right).

In Fig. 3, mid and bottom, we highlight Γ_{cl} and Γ_{op} in red and green, respectively; in Fig. 3, mid, we color with pale gray the part of the first level set φ excluded by the auxiliary level set function ψ and with dark gray the zero level of the function ψ_{op}. We remark that, the repetition of the points distally in the case of the open leaflet ensures a continuity in the direction of the z-axis to the level set φ_{op} (Fig. 3, mid-center). In Fig. 3, bottom, as example of the reliability of our method, we show the final closed and open valve superimposed to the 3D-CE-CT images.

4.4 Mesh generation

The computational mesh for our simulations is constructed starting from the output of the segmentation method, i.e., the triangular surface representing the aortic lumen (Fig. 2, right), consistently rotated according to the reference system defined for the implicit surfaces Γ_{cl} and Γ_{op}.

As first step, we crop the coronary arteries from the model interpolating the resulting hole with a thin plate spline. Then, the surface is cut by planes perpendicular to the lumen longitudinal axis at the left ventricle and at the aortic arch in order to create the inlet and the outlet section, respectively (Fig. 4, top-left). To minimize the sensitivity to the boundary conditions that we set, straight flow extensions are added to the inlet and outlet faces of the model. The fluid domain is then created filling the resulting surface with linear tetrahedra with the tool described in Faggiano et al. (2013b) and

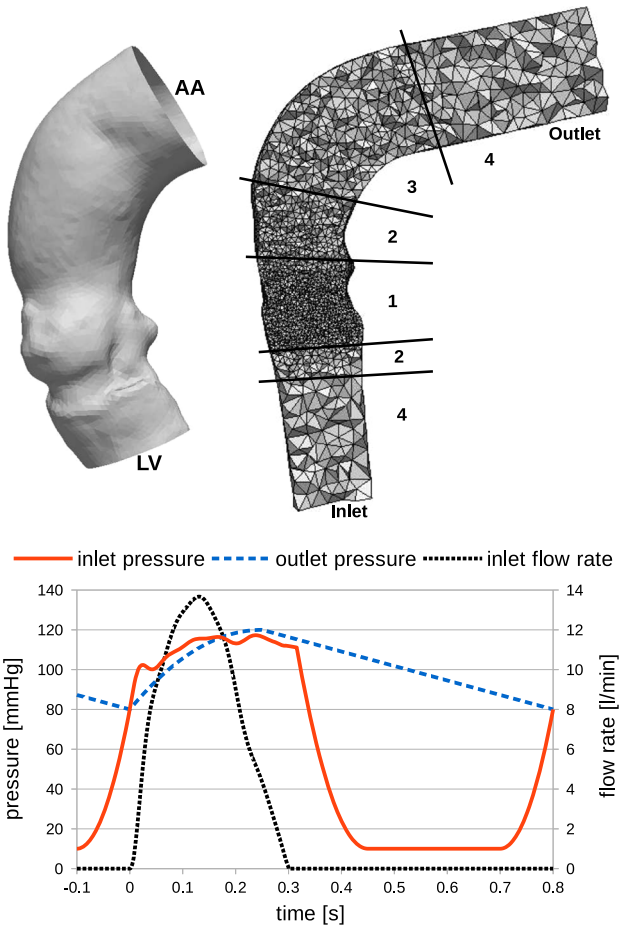

Fig. 4 Processed aortic lumen surface (*top-left*), opened at the left ventricle (LV) and at the aortic arch (AA); an example of a coarse tetrahedral mesh with flow extensions characterized by four different regions of refinement (*top-right*); the boundary conditions for one heart beat (*bottom*)

implemented in the vascular modeling toolkit (vmtk[1]). In particular, we first define four regions on the surface: a region near the valve (region 1), a buffer region around the first one (region 2), a third region representing the residual ascending aorta (region 3), and a fourth region representing the flow extensions (region 4). For each of these regions, we set a different mesh refinement obtaining a highly refined mesh in the first region and three different refinements in the other three regions gradually coarsening while moving away from the valve; we show in Fig. 4, top-right, an example of this type of refinement in a coarse mesh made of 10^5 tetrahedra. The mesh used for the numerical simulations is comprised of 2.31×10^6 tetrahedra, with a mean mesh size in the four regions equal to 0.21 , 0.27 , 0.41 and 0.5 mm, respectively; in detail, the valvular region (region 1) comprises 0.9×10^6 tetrahedra, while the regions 1, 2 and 3 comprise 1.8×10^6 tetrahedra.

[1] http://www.vmtk.org.

4.5 Boundary conditions

The boundary conditions of the AV-RIIS model are two pressure profiles, p_{in} for the inlet $\partial\Omega_{\text{in}}$ and p_{out} for the outlet $\partial\Omega_{\text{out}}$ [see Eq. (15)]. Concerning the outlet pressure profile p_{out}, since clinical data are not available, we prescribe an idealized pressure behavior similar to the ones in Korakianitis and Shi (2006) and Astorino et al. (2012) with a minimum pressure value of 80 mmHg at the beginning of the systole (when the left ventricle pressure overcomes the aortic pressure) and a maximum pressure of 120 mmHg at late systole (Fig. 4, bottom, dashed blue curve). Concerning the inlet pressure profile p_{in}, we take advantage of the available patient-specific data, i.e., the maximum flow rate measured by ultrasound. To this aim we proceed as follows:

1. We perform a first simulation with a fixed open valve (for which $\mathcal{K} = 1$) prescribing at the inlet the flow rate profile of Avolio (1980) rescaled in order to obtain the maximum patient-specific flow rate (Fig. 4, bottom, dotted black curve). To prescribe this flow rate, a Dirichlet boundary condition with a flat velocity profile is imposed on the inlet $\partial\Omega_{\text{in}}$ (Faggiano et al. 2013a; Bonomi et al. 2015). In order to work with regime values of pressure and velocities, we run this simulation for three heart beats.
2. We obtain the systolic pressure profile $p_{\text{in}}^{\text{sys}}$ as result of the last heart beat at the inlet.
3. We build the full inlet pressure profile p_{in} (Fig. 4, bottom, continuous red curve) as follows: when $t \in [-0.1, 0]s$ we set an exponential function interpolating the values 10mmHg and 80mmHg to reproduce the isovolumetric contraction phase of the left ventricle. Then, starting at $t = 0s$ we impose the systolic pressure profile $p_{\text{in}}^{\text{sys}}$; this profile is imposed for the whole systole until the valve is completely closed ($t = t_{\text{cl}}$). We remark that the time t_{cl} (in our simulation equal to 0.316 s) is not fixed a priori but depends on the solution of the AV-OD model. Finally, for $t \in [t_{\text{cl}}, t_{\text{cl}} + 0.1]s$ we set an exponential function to interpolate the value of pressure at t_{cl} and the value of 10mmHg, which represents the idealized left ventricle diastolic pressure (Korakianitis and Shi 2006).

We finally remark that the choice of an inlet pressure boundary condition in place of the Dirichlet boundary condition on the velocity is necessary to properly model the evolution of the pressure in the domain along the whole cardiac cycle and particularly the pressure jump across the closed leaflets at diastole.

5 Results and discussion

In order to highlight the capability of our framework to reconstruct the patient-specific leaflets, we report in Fig. 5 three different views of the systolic 3D-CE-CT image of the patient with the reconstructed open valve superimposed: Our aortic valve reconstruction method captures the complex geometry of the leaflets, following its curvatures and irregularities. More in detail, the polynomial fitting of the clouds of points (see Sect. 4.3, Fig. 3) is obtained by a least-square algorithm. The results are characterized by the following coefficients of determination R^2: an average R^2 equal to 0.918 and 0.912 for the polynomials corresponding to ϕ_{cl} and ϕ_{op}, respectively; R^2 is equal to 0.985 and 0.965 for ψ_{cl} and ψ_{op}, respectively. The worst case exhibits the value $R^2 = 0.865$ correspondingly to $\phi_{L,\text{op}}$.

As it can be appreciated also from Fig. 3, in the open position the studied leaflets are clearly asymmetrical in both their shape and position with respect to the aortic root: the non-coronary leaflet is almost straight and attached to the wall (Fig. 5, left and center); the right-coronary leaflet is characterized by a large space behind it (the right-coronary sinus) and it assumes a standard configuration (Sturla et al. 2013) with two changes in curvature and a profile completely convex toward the sinus (Fig. 5, left and right); on the contrary, the left-coronary leaflet appears to be not fully opened and assumes an almost straight configuration in the left-non and right-left views (Fig. 5, center and right). These differences are physiological and are specific to this patient. As also highlighted in Faggiano et al. (2013a), Della Corte et al. (2012) and Bonomi et al. (2015), leaflets opening restrictions or asymmetries can influence the flow direction and the generation of helical flow patterns making the patient-specific aortic valve reconstruction an important step toward patient-specific simulations of the aorta (Marom 2015).

Concerning the numerical simulation, we implement our model in the LifeV library[2]. In particular, the library provides an efficient and flexible parallel framework (based on the *openMPI* standard) to assemble the FE matrices and uses the Trilinos library[3] to deal with preconditioning and resolution of the linear system; see in particular the FSI solvers in Crosetto et al. (2011), Deparis et al. (2016), and Tricerri et al. (2015). The results that we show in this section are obtained running the simulations on a cluster using 192 CPUs, with a mesh composed of 1.5×10^6 degrees of freedom. We set the blood dynamic viscosity $\mu = 3.5 \times 10^{-3}$ g/(mm s) and the blood density $\rho = 10^{-3}$ g/mm^3. We choose the time step equal to 2×10^{-4} s; for time independency, we find that when doubling the time step, the results are not affected by appreciable changes.

[2] www.lifev.org.

[3] www.trilinos.org.

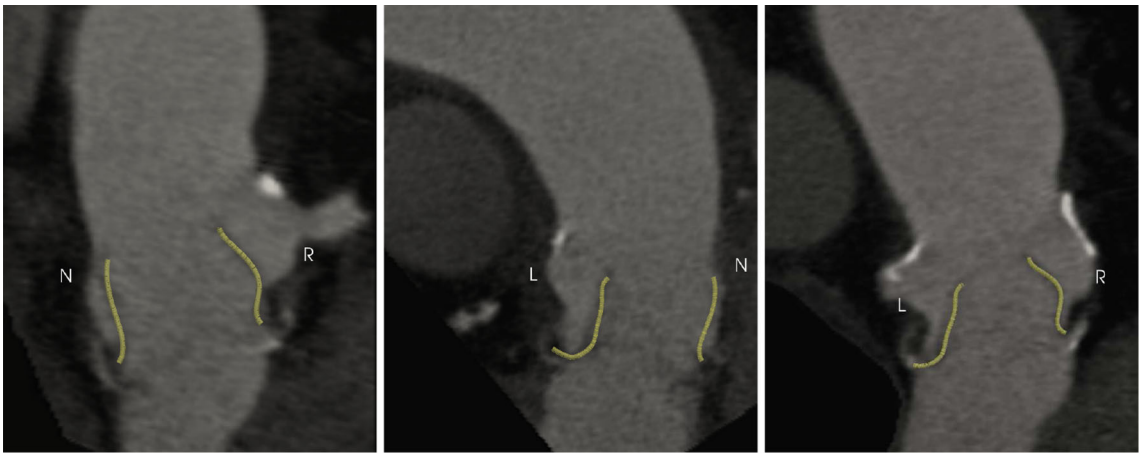

Fig. 5 Systolic 3D-CE-CT image of the patient sliced along the non-coronary/right view (*left*), left/non-coronary view (*center*) and left/right view (*right*). The reconstructed open valve is superimposed in bright color. The left (L), the right (R) and the non-coronary (N) sinuses of Valsalva are indicated

Concerning the parameters of the AV-RIIS model, we set the resistance $R_\Gamma = 10^6\,\mathrm{g/(mm\,s)}$ to weakly enforce the no-slip condition on the leaflets of the valve, even in case of an high pressure gradient across them. We have observed that a smooth regularized Dirac function δ_ε [Eq. (10)] featuring a support across three mesh elements guarantees an effective resistive term, thus avoiding flow penetration across the leaflets. Consequently, since δ_ε has a 2ε-wide support, we suggest to set the value of ε at least 1.5 times the mean mesh size of the valvular region which in our case is about 0.21 mm; then ε is equal to 0.4 mm which roughly corresponds to valve leaflets 0.8 mm thick. We also remark that, if ε increases, the matrix condition number decreases, but the valve becomes thicker and thicker. As a general guideline, we therefore suggest to consider a fine mesh in the valvular region in order to set a sufficiently small ε reproducing a physiological value of the valve thickness. In particular, the thickness of a healthy valve changes with the age; for people beyond 60 year old as the patient under investigation, it ranges between 0.5 and 1.4 mm (Sahasakul et al. 1988). Concerning the two control volumes (subdomains) Ω_{lv} and Ω_{ao} used to compute the variables P_{lv} and P_{ao} (Eq. (20)), we cut the vessel perpendicularly to the centerline obtaining two 3 mm-thick regions placed 10 mm far from the bottom and the top part of the valve, respectively. We found that the numerical results of the AV-0D model are not significantly affected by the location of these two control volumes provided that these lay at distances between 5 and 25 mm from valve.

In Fig. 6 we show the evolution of the quantities involved in the AV-0D model [P_{lv}, P_{ao} and Q_{ao} of Eq. (20)] and the evolution of the valvular angle and of the orifice area: The leaflets start the opening stage when the pressure in the upstream control volume (at the end of the left ventricle) overcomes the one measured downstream (in the aortic root); on the contrary, the closing procedure starts when the downstream pressure exceeds again the upstream pressure at $t = 0.251$ s, although the flow rate is still positive for further 65 ms. This behavior is obtained in virtue of the inclusion of the AV-0D model in our method. Indeed, as opposed to other full 3D-FSI approaches (Hsu et al. 2014; Kamensky et al. 2015; Hart et al. 2003b; Borazjani et al. 2010), our AV-RIIS model is independent on the choice of the stress-free config-

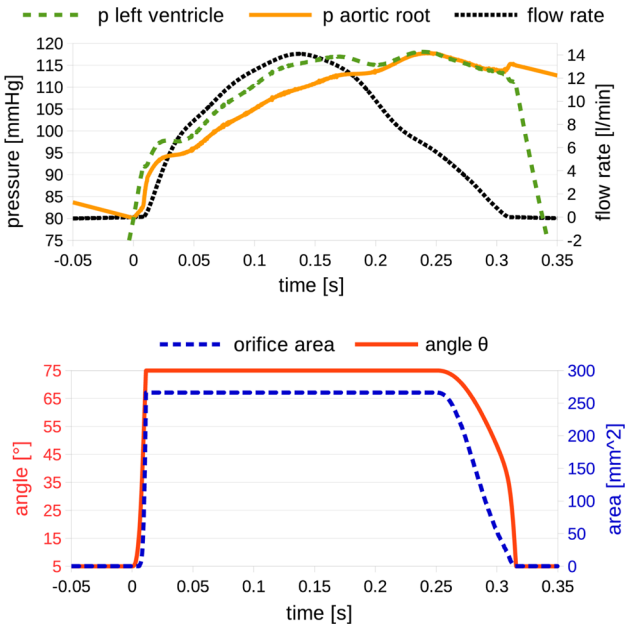

Fig. 6 Evolution, during systole, of the quantities driving the AV-0D model (*top*): the pressure in the control volumes taken upstream ('p left ventricle', *dashed green line*) and downstream ('p aortic root', continuous orange line) the aortic valve, and the flow rate at the inlet ('flow rate', *dotted black line*). Evolution (*bottom*) of the valvular angle ϑ (*continuous red line*) and of the orifice area (*dotted blue line*)

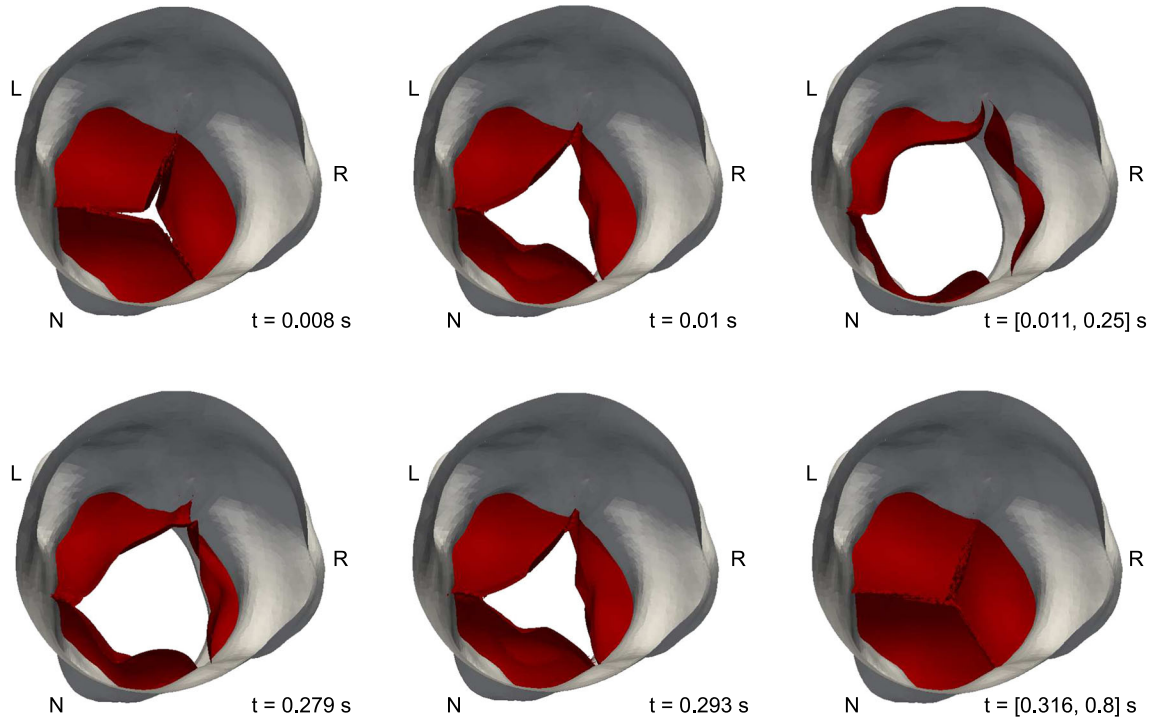

Fig. 7 Top view of the aortic valve shape in some instants of the cardiac cycle: opening valve (*top*) and closing valve (*bottom*). The left (L), the right (R), and the non-coronary (N) sinuses of Valsalva are indicated

uration of the valve. As also highlighted by Marom (2015), this choice remains a controversial aspect in case of patient-specific simulations since a stress-free configuration might not exist in native valves; nevertheless, handling this critical aspect is not required by our simplified formulation.

In a physiological aortic valve, the evolution of the orifice area during the systole can be divided into three stages (Leyh et al. 1999; Handke et al. 2003; Steenhoven et al. 1981): a rapid opening phase, a slow closure with very small changes of the orifice area, and a rapid closure. The general trend reproduced by our model (Fig. 6, bottom) coincides with this three-stage behavior described in the in vivo studies (Leyh et al. 1999; Handke et al. 2003; Steenhoven et al. 1981) with the slow closure approximated by a fixed valve position, as expected by the AV-0D model (Korakianitis and Shi 2006). The duration of the opening and closing phases is of 11 ms and 65 ms, respectively, which are times comparable to the ones shown by the AV-0D model of Korakianitis and Shi (2006). On the contrary, the in vivo measurements generally show a slower opening phase (Leyh et al. 1999; Handke et al. 2003): in particular, the study of Handke et al. (2003) shows average opening and closing times of 76 ± 30 and 42 ± 16 ms, respectively. The fact that the opening stage is faster than the realistic one induces an high valve velocity $\boldsymbol{u}_\Gamma$ leading to some numerical instability: for this reason we consider in our model $\boldsymbol{u}_\Gamma = \boldsymbol{0}$, a choice which affects the fluid behavior only in a limited manner and only during the fast valve opening. We remark that this limitation does not prevent the valve to move since the solution ϑ of the AV-0D model only depends on the values of P_{lv}, P_{ao}, and Q_{ao} which are independent of valve velocity $\boldsymbol{u}_\Gamma$. Thus, setting $\boldsymbol{u}_\Gamma$ equal to zero in the transitory phase introduces a quasi-static approximation of the valve dynamics: the leaflets change their position deviating correctly the flow along the aorta, but formally violating the adherence of the blood to the displacing valve, even if only for a limited time interval of the heartbeat.

The dynamics of the valve is visualized in Fig. 7, where a sequence of snapshots in time over the cardiac cycle is shown. The configurations assumed by the orifice while the valve is moving are qualitatively in agreement with the shapes reported in in vivo studies (Steenhoven et al. 1981; Handke et al. 2003), thus demonstrating the capability of our method to reproduce the intermediate valve shapes between the patient-specific open and closed positions. More in detail, during the opening phase, the shape starts from a stellate configuration (Fig. 7, top-left) and becomes triangular (Fig. 7, top-center) and then circular at the maximum opening (Fig. 7, top-right); during the closing procedure, the shape of the valve changes toward a triangular morphology (Fig. 7, bottom-left and bottom-center). Finally, at the end of the systole and during the whole diastole the valve is completely closed (Fig. 7, bottom-right). Such behavior is also observed, for instance, by Ranga et al. (2006), in a simulation performed in a symmetric and idealized geometry; on

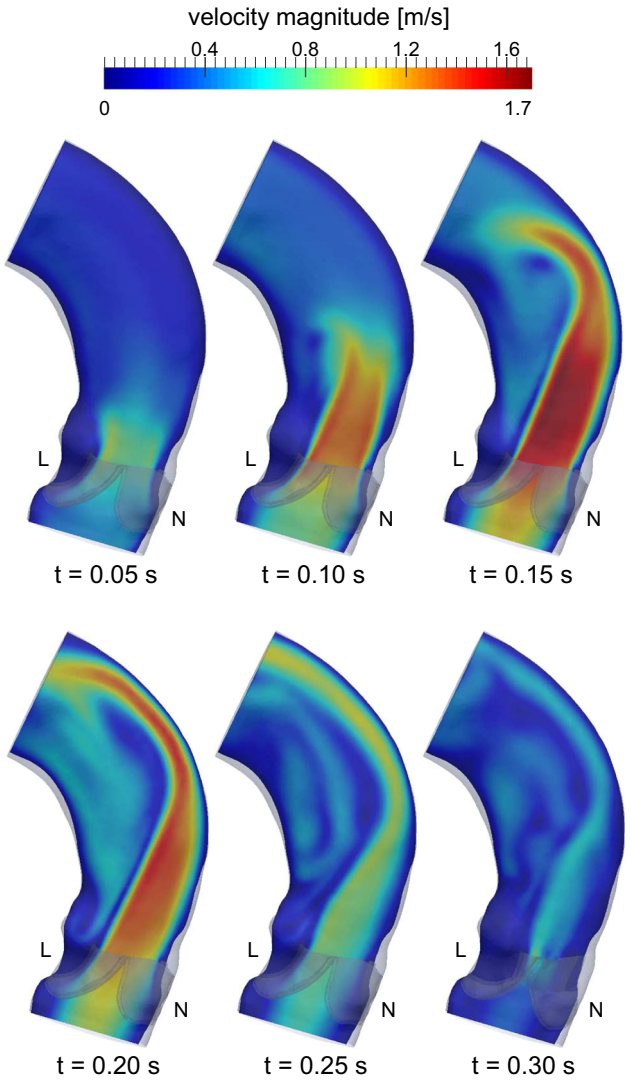

Fig. 8 Velocity magnitude contours depicted on a long-axis slice passing by the left (L) and the non-coronary (N) Valsalva sinuses, at six different time instants during systole. The aorta and the leaflets are shown in transparency

the contrary, our patient-specific geometry leads to an asymmetric shape of the orifice resulting more similar to the in vivo images shown by Handke et al. (2003).

In Fig. 8, we show contours of the velocity magnitude on a long-axis slice at six different time instants during the systole, with the leaflets visible in transparency.

First, we remark the performance of our method, since the velocity remains practically null on the leaflets even when the maximum velocity magnitude of about 1.7 m/s is reached. The position of the slice passing by the left and the non-coronary sinus allows to analyze the deviation of the flow from the aortic centerline: It is evident that the patient-specific valve geometry influences the flow direction generating an asymmetric jet which impacts the aortic wall at the systolic peak (Fig. 8, top-right). Such flow deviation starts to be visible from the end of the early systole (Fig. 8, top-center) and becomes more and more evident at late systole (Fig. 8, bottom). We emphasize the importance of using the patient-specific geometry of the leaflets in order to obtain such results (Marom 2015); we stress the concept that an idealized symmetric geometry for the aortic root, or even only for the three leaflets, can not capture such complex dynamics of the blood flow (Borazjani et al. 2010; Hsu et al. 2014; Ranga et al. 2006).

In Fig. 9, we show at four different times of the cardiac cycle the blood pressure on the same long-axis slice of Fig. 8 and inside the volumetric mesh nearby the left coronary leaflet for $\varphi \in [-0.6, 0.6]$. The pressure field during the opening of the valve, at the early systole, is visible in Fig. 9 ($t = 0.01$s): in this phase the pressure in the left ventricle and in the aortic root is almost homogeneous, with the highest pressure gradient localized among the leaflets. The zoom inside the mesh nearby the left coronary leaflet enhances the localization of the pressure drop in the interior part of the valve, while the external part of the leaflet is characterized by a constant pressure.

At the systolic peak (Fig. 9, $t = 0.15$ s), we can draw similar considerations concerning the pressure distribution in the left ventricle and in the sinuses of Valsalva, while the situation drastically changes in the ascending aorta. Indeed, the deviation of the flow underlined in Fig. 8, top-right, induces a corresponding pressure peak near the wall and, as a consequence, a depression zone in the central part of the ascending aorta. However, in this phase, the pressure in the left ventricle is higher than the average pressure in the aortic root and the valve remains fully open. On the contrary, at the late diastole we notice the opposite situation (Fig. 9, $t = 0.30$ s): the blood slows down and, despite the flow rate is still positive, the pressure gradient inverts its direction leading to the valve closure. The depression zone is still present in this phase, coherently with the persistent flow deviation (Fig. 8, bottom-right). In Fig. 9 ($t = 0.50$ s), we show an instant of the diastolic phase characterized by the high pressure jump of more than 90 mmHg across the leaflets. By looking at the volumetric mesh of the left coronary leaflet, it is interesting to note how the sharp pressure jump is localized in a region of thickness 2ε corresponding to about three mesh elements, i.e., basically where the RIIS resistive term extend its action; on the contrary, outside this region, the pressure is not affected by this high pressure jump taking values with small oscillations around the lowest and the highest values of the color legend. More in general, looking at the four volumetric meshes nearby the left coronary leaflet shown in Fig. 9, bottom, we notice the ability of our method in reproducing the presence of the valve using the resistive RIIS term and, as a consequence, without the necessity of meshing the valve surface; indeed, the movement of the leaflets does not mod-

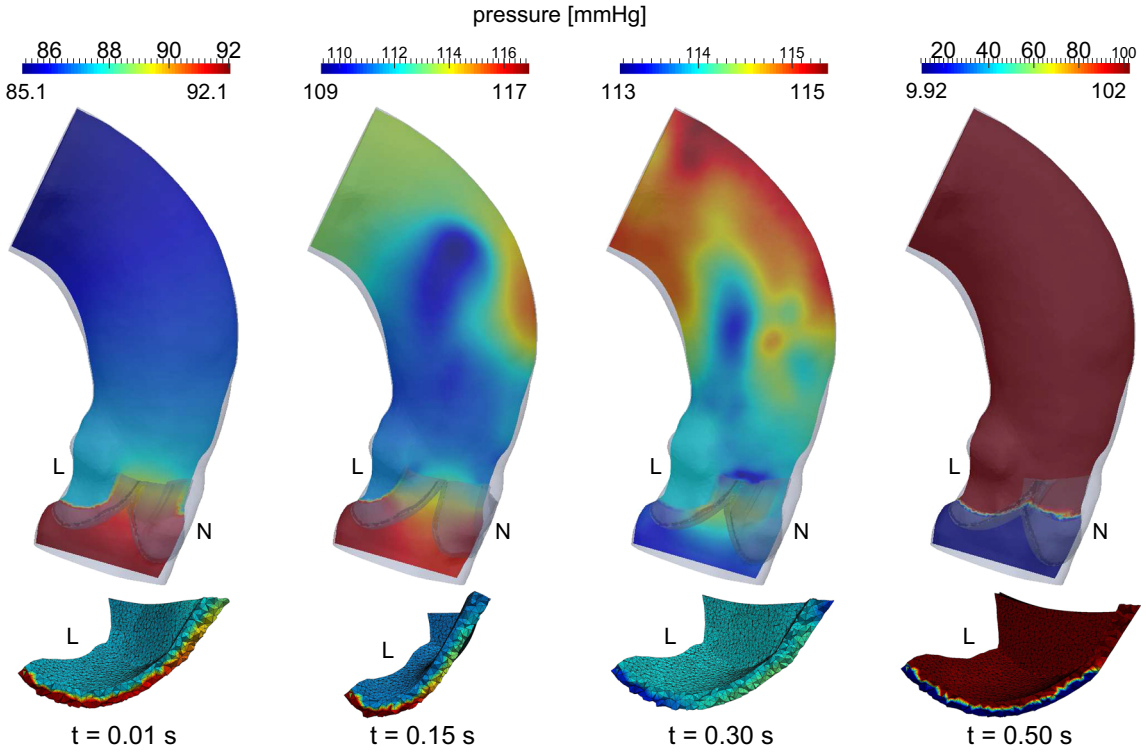

Fig. 9 Blood pressure at four different times during the cardiac cycle: pressure depicted on a long-axis slice passing by the left (L) and the non-coronary (N) Valsalva sinuses and on the volumetric mesh zoomed nearby the left coronary leaflet, where the level set function $\varphi \in [-0.6, 0.6]$ at the current time

ify the computational mesh, but it is totally described by the evolution of the two level set functions φ and ψ through our method.

With the aim of showing the evolution of the 3D vortex structures in the aorta, we show in Fig. 10 the Q-criterion (Hunt et al. 1988) normalized for its maximum value at each time instances and the velocity streamlines. Concerning the early systole, the Q-criterion shows a ring detaching and then breaking away from the three leaflets (Fig. 10, top); this highlights well organized laminar vortex structures in this phase of the cardiac cycle. It is interesting to note the asymmetry of the ring that evolves mainly in the two coronary sinuses rather than in the non-coronary one; indeed, since the aortic wall is almost attached to the non-coronary leaflet, the vortexes do not have sufficient space to develop in this sinus. The ring visualized by the Q-criterion in early systole is also discussed by Borazjani et al. (2010), where the authors also underline that in an anatomic aorta the ring is asymmetric rather than symmetric as it would occur in an idealized aorta. At this stage of the cardiac cycle, the movement of the vortex from the right and left coronary sinuses to the ascending aorta is clearly visible also by looking at the streamlines (Fig. 10, bottom-left and bottom-center). As reported in Charitos and Sievers (2013), these vortexes also help the leaflets not to attach to the aortic wall. During the central part of the systole, when the flow rate and the velocity magnitude reach their peak values, the vortex structures break down into smaller structures (Fig. 10, center-left); a similar behavior is commented in Borazjani et al. (2010). Looking at the streamlines (Fig. 10, bottom-right) we notice how, in this phase, a disorganized recirculation appears at a bigger scale, localized in the region of the aorta opposite to the non-coronary sinus: this phenomenon contributes to the deviation of the blood jet to the wall, as noticeable in Fig. 8 by observing the velocity magnitude. At the late systole, when the velocity decreases again, the size of vortex structures increases and their localization in the opposite region of the non-coronary sinus is more evident (Fig. 10, center-center). Finally, the patterns assumed by the Q-criterion during the diastole are particularly interesting (Fig. 10, center-right): A big cylindrical shape appears in the ascending aorta indicating an organized recirculation, while two helical patterns appear only in the two coronary sinuses indicating the presence of vortexes; as reported in Charitos and Sievers (2013), these vortexes are physiological and contribute to the closure of the leaflets and to the perfusion of the coronary arteries. We remark that our computational framework allows capturing both physiological and pathological behaviors, a feature that would have not been possible by using simplified geometrical configurations of the valve.

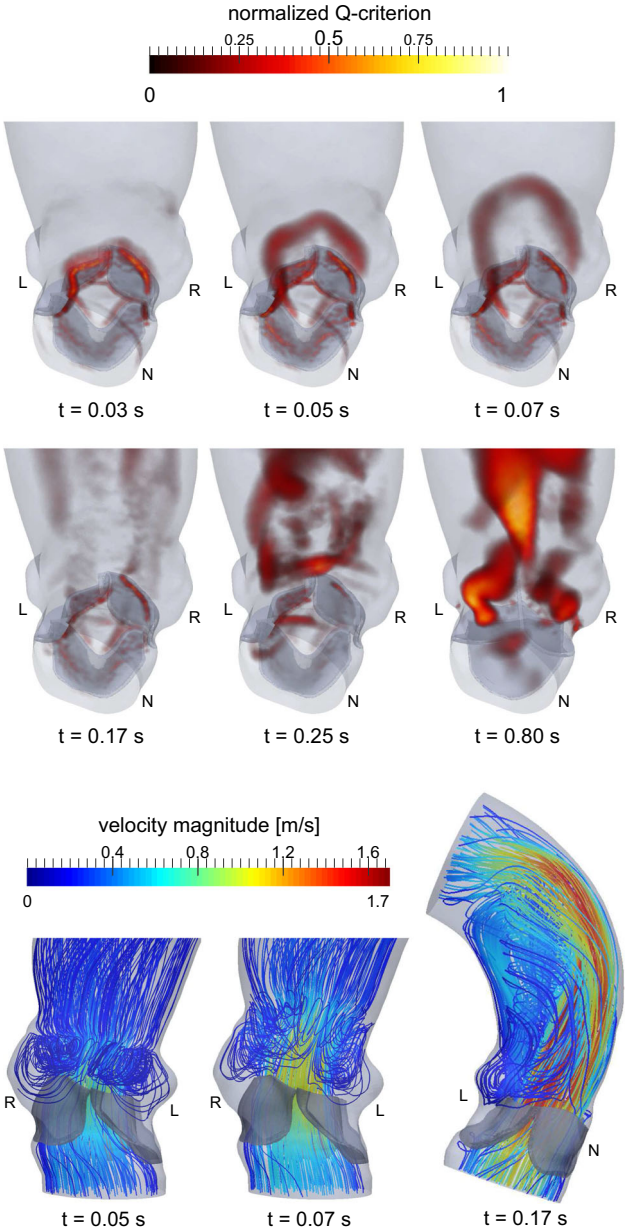

Fig. 10 Vortex structures visualized by a volume rendering of the normalized Q-criterion at different instants of the cardiac cycle (*top*); on the bottom streamlines of the velocity: the evolution of the vortexes in the right and left coronary sinuses during the early systole (*left and center*), and the systolic peak in the ascending aorta (*right*). The aorta and the leaflets are imaged in transparency and the left (L), the right (R) and the non-coronary (N) Valsalva sinuses are indicated

Comparison with basic aortic valve models In Fig. 11 we report images of flow patterns at the systolic peak ($t = 0.15$ s) and during the closing phase ($t = 0.28$ s) for simulations performed using three aortic valve models with increasing complexity: the simplest model (Fig. 11, left, "without valve") consists in totally neglecting the valve; the intermediate one (Fig. 11, center, "fixed valve") consists in including a fixed open valve thus neglecting its dynamical effects; the most complex one (Fig. 11, right, "moving valve") is our full model that includes the movement of the valve. The geometry of the aorta, of the leaflets (when used), and the inlet flow rate are the same in the three cases.

The flow pattern generated by the model "without valve" is significantly different compared to the others; indeed, in this case the maximum velocity magnitude is cut almost by a factor two and the flow patterns are mostly symmetric with respect to the centerline. Concerning the "fixed valve" and the "moving valve" models, almost negligible differences can be noted at the systolic peak, while slightly different flow patterns can be distinguished during the valve closure. Therefore, in order to better quantify the differences between these three models, we compute two fluid dynamics indexes across three slices orthogonal to the aorta centerline: the flow reversal ratio (FRR) index (Faggiano et al. 2013a)—which measures the percentage of retrograde flow rate with respect of the forward-directed flow rate—and the normalized flow asymmetry (NFA) index (Sigovan et al. 2011; Faggiano et al. 2013a), which quantifies flow eccentricity varying from NFA $= 0$ when the center of forward velocity coincides with the center of the vessel (symmetric flow) to NFA $= 1$ when the center is on the vessel wall (totally asymmetric flow). The position of the slices and the values of the indexes are reported in Table 2.

The indexes computed for the model "without valve" clearly indicate that the absence of the patient-specific leaflets affects the blood flow dynamics. Indeed, at the systolic peak, the flow is completely forward-directed (FRR $\simeq 0.0\,\%$) and totally centered (NFA $\simeq 0.0$) without the inclusion of the leaflets, while with the patient-specific leaflets there is a systolic vortex which causes a positive FRR (varying from 8 % on slice 1–19 % on slice 3) and an evident deviation of the flow toward the wall (NFA $\simeq 0.3$).

When comparing the "fixed valve" and the "moving valve" models, we notice very similar values at the systolic peak, demonstrating that the two models behave similarly during this phase that is crucial in clinical application. More in details, we found a difference of FRR equal to 3.6 % on slice 1, 0.2 % on slice 2, 5.1 % on slice 3 and a difference of NFA equal to 1.2 % on slice 1, 0.2 % on slice 2 and 2 % on slice 3. On the contrary, during the closing procedure, the indexes present larger discrepancies: At $t = 0.28$ s we found a difference of FRR equal to 14.7 % on slice 1, 18.4 % on slice 2, 13.7 % on slice 3 and a difference of NFA equal to 8.9 % on slice 1, 10 % on slice 2 and 4.5 % on slice 3. However, these differences can not be considered significant with respect to the intrinsic uncertainty of the aorta-valve model.

We remark that these comparisons highlight the importance of using a detailed valve model, even if a more rigorous study should involve a large set of patients.

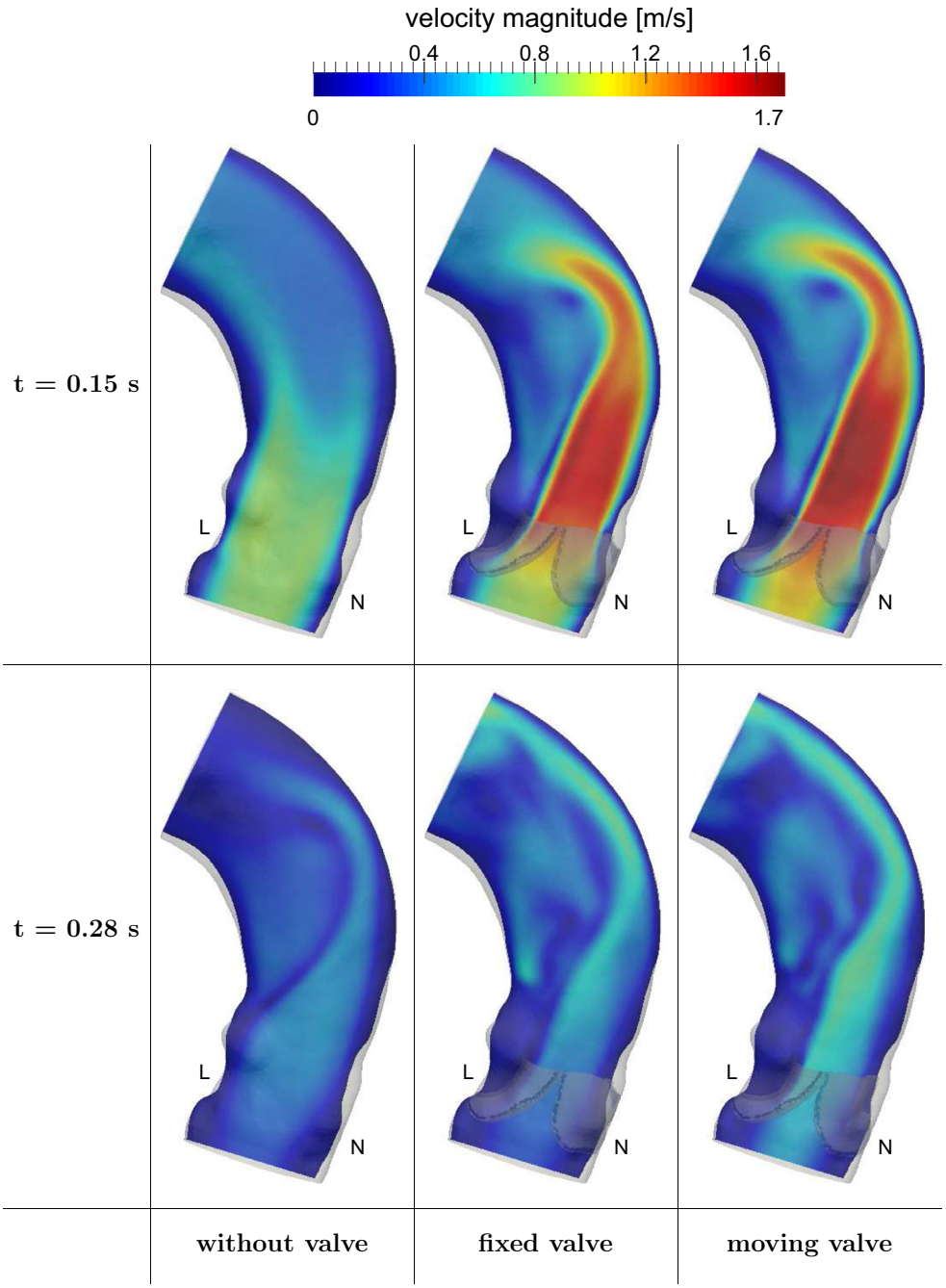

Fig. 11 Comparison of the velocity magnitude contours depicted on a long-axis slice passing by the left (L) and the non-coronary (N) Valsalva sinuses, for models "without valve" (*left*), with a "fixed valve" (*center*), and with a "moving valve" (*right*). Results are shown at the systolic peak ($t = 0.15$ s) and during the closing phase ($t = 0.28$ s). The aorta and the leaflets are shown in transparency

6 Conclusions

In this paper, a full computational framework to simulate patient-specific hemodynamics in the aorta with patient-specific aortic valve is presented. The framework includes a segmentation method for the aorta and a valve reconstruction method able to obtain the closed and the open configurations of the patient-specific valve. The fluid dynamics problem with the inclusion of the valve is solved by a new resistive immersed implicit surface model (AV-RIIS). Our model is based on an analytical implicit representation of the valve leaflets through a level set formulation. The presence of the valve is then included in the momentum equation of the Navier–Stokes equations by adding a resistive term, which weakly enforces the blood to adhere to the leaflets (Fernández et al. 2008; Astorino et al. 2012). The model is then

Table 2 FRR index (in %) and NFA index at systolic peak ($t = 0.15\,s$) and during the closing phase ($t = 0.28\,s$), for models "without" valve, with a "fixed" valve, and with a "moving" valve

Time	Slice	FRR [%]			NFA		
		Without	Fixed	Moving	Without	Fixed	Moving
0.15 *s*	1	3.755	8.313	8.025	0.126	0.314	0.311
	2	0.002	13.43	13.40	0.021	0.291	0.290
	3	0.000	20.00	19.03	0.030	0.383	0.375
0.28 *s*	1	36.14	27.23	23.74	0.135	0.204	0.223
	2	31.34	36.10	30.49	0.195	0.191	0.212
	3	44.96	40.74	35.82	0.322	0.517	0.495

Slices at which indexes are evaluated are depicted on the right

enriched by coupling the AV-RIIS with a reduced 0D model (Korakianitis and Shi 2006) to reproduce the movement of the valve between its closed and open positions; we named this model "reduced 3D–0D FSI model". In this framework, the coupling between the 3D and 0D models is performed through an original algorithm which allows to obtain realistic physiological results. At the discrete level, a FE formulation is used to spatially approximate the Navier–Stokes equations with an extended SUPG stabilization (Bazilevs et al. 2007; Forti and Dedè 2015).

We applied our computational framework to the analysis of blood flow in a patient enrolled by Ospedale Sacco of Milano, Italy. The results showed that the framework succeeded in the reconstruction of the patient-specific aortic valve leaflets in both open and closed positions: This is a very challenging and important aspect in numerical models for the aortic valve, since the geometrical configuration of the valve greatly influences the hemodynamics (Marom 2015). Indeed, patient-specific aortic leaflets in open and closed configurations were not included so far in the literature as they are usually idealized (Borazjani et al. 2010; Borazjani 2013; Hart et al. 2003a, b, 2004; Le and Sotiropoulos 2013; Ge and Sotiropoulos 2010; Kamensky et al. 2015; Hsu et al. 2014). To the best of our knowledge, the work of Astorino et al. (2012) is the only one that includes patient-specific valves in open and closed configurations even if only within an "on–off" strategy which neglects transitory, intermediate effects between these configurations. In this respect, our AV-RIIS method represents a step forward, also in consideration of the fact that the leaflet reconstruction method is simple (thanks to the polynomial fitting), versatile in pathological cases (as it avoids the use of template meshes and mapping techniques), and computationally efficient (in virtue of the implicit functions tracking the leaflets which avoid the construction of volumetric meshes of the valve). Moreover, we highlighted the ability of our method to reproduce the motion of the orifice and of the leaflets position during the cardiac cycle. Concerning the pressure field inside the aorta, the results demonstrated that the method is capable of capturing the sharp pressure jump across the valve without the necessity of meshing the valve leaflets. The recovered velocity field evidenced an asymmetric fluid pattern, which is strictly linked to patient-specific geometric asymmetries, captured thanks to our method, as also highlighted by the comparison with simulations performed without the inclusion of the leaflets.

In summary, we demonstrated the importance of counting on a framework which is capable of simulating blood flow through a patient-specific aortic valve; as a matter of fact, even more sophisticated approaches used for the same patient-specific geometry—but with idealized leaflets—could hardly grasp the asymmetrical hemodynamics characterizing the patient as demonstrated in Faggiano et al. (2013a), Bonomi et al. (2015), Wendell et al. (2013), Della Corte et al. (2012). The variability among different patients can be captured only considering the patient-specific aortic geometry and the patient-specific leaflets in the correct position. Being our proposed framework independent of any a priori assumption on the shape of the leaflets, it can be used for both physiological and pathological cases, the latter being the most significant for clinicians. We remark that pathological cases involve a large geometric variability of the valve (e.g., the bicuspid valve can assume five different principal configurations), thus demanding for versatile computational tools, a requisite that our computational framework addresses by means of the newly proposed reconstruction approach of the valve leaflets. The analysis reported in this work is purely demonstrative of the ability of our method, and we did not provide any clinical interpretation of the numerical results associated with the patient; however, since our reduced 3D–0D FSI model is conceived to work on patient-specific data, it can be used to better understand the hemodynamics of the ascending aorta, as well to study aortic and valvular diseases. In these cases, a complete sensitivity study must be performed on the choice of the grid size in relation to clinical indicators.

We stress the fact that our reduced 3D–0D FSI model involves the coupling of a detailed model for the fluid dynamics of the blood with a simplified, kinematic model for the

valve. The latter model— called AV-0D—is too simplistic to yield detailed information on the mechanical behavior of the valve itself, as e.g., on local strains and stresses. Indeed, the main goal of our computational framework is to take into account for the valve effects onto the blood flow. Furthermore, in the current model we assumed rigid arterial walls for the aorta, thus neglecting the interaction between fluid and aortic wall structure; however, this can be easily taken into account by extending the RIIS approach to a fluid–structure model of the aorta. Concerning the leaflets, more sophisticated mechanical models of the valve can be used in place of the purely geometric AV-0D model by Korakianitis and Shi (2006) and coupled with the AV-RIIS model for the fluid, yet maintaining the level set description of the immersed valve.

A further limitation of the current work is the dependency of the valve behavior in the AV-0D model on the parameters proposed in Korakianitis and Shi (2006), which, for the patient at hand, produces a very fast opening stage of the valve. Tuning the parameters to match the real valve velocity at the opening and closing stages is a possibility, even if, for the patient under consideration, their measurements or even estimates were not possible. In this respect, a further development of this work would consist in setting the parameters involved in the AV-0D model to obtain physiological valve behaviors; we remark however that this fitting should be performed on a large set of patients.

Moreover, we remark that the very fast opening of the valve induces large values of the velocity u_Γ which, without suitable smoothing or regularization procedures of the level set function representing the leaflet, leads to numerical instabilities. We overcame this problem by setting $u_\Gamma = 0$ in Eq. (28), a simplification that introduces a quasi-static approximation of the valve dynamics. Albeit this formally represents a violation of the physical adherence of the blood to the moving valve, we believe that the effect of our approximation is very limited in time along the heartbeat and in space in the aortic root.

Acknowledgements We gratefully acknowledge M.D. S. Ippolito and M.D. R. Scrofani (Cardiac Surgery Department of Ospedale Sacco, Milano, Italy) for the clinical data used in this paper and Dr. S. Deparis, Dr. D. Forti and Dr. A. Laadhari (CMCS, École Polytechnique Fédérale de Lausanne, Lausanne, Switzerland) for assistance and suggestions.

Appendix: Benchmark problems for the RIIS model

We consider two bidimensional test problems taken from the literature and use them as benchmark tests for the treatment of rigid body motion in a fluid using the RIIS approach described above.

The first benchmark problem is the oscillating cylinder by Wan et al. (2004): It consists of a prescribed sinusoidal motion around the center of a rectangle and with a no-slip

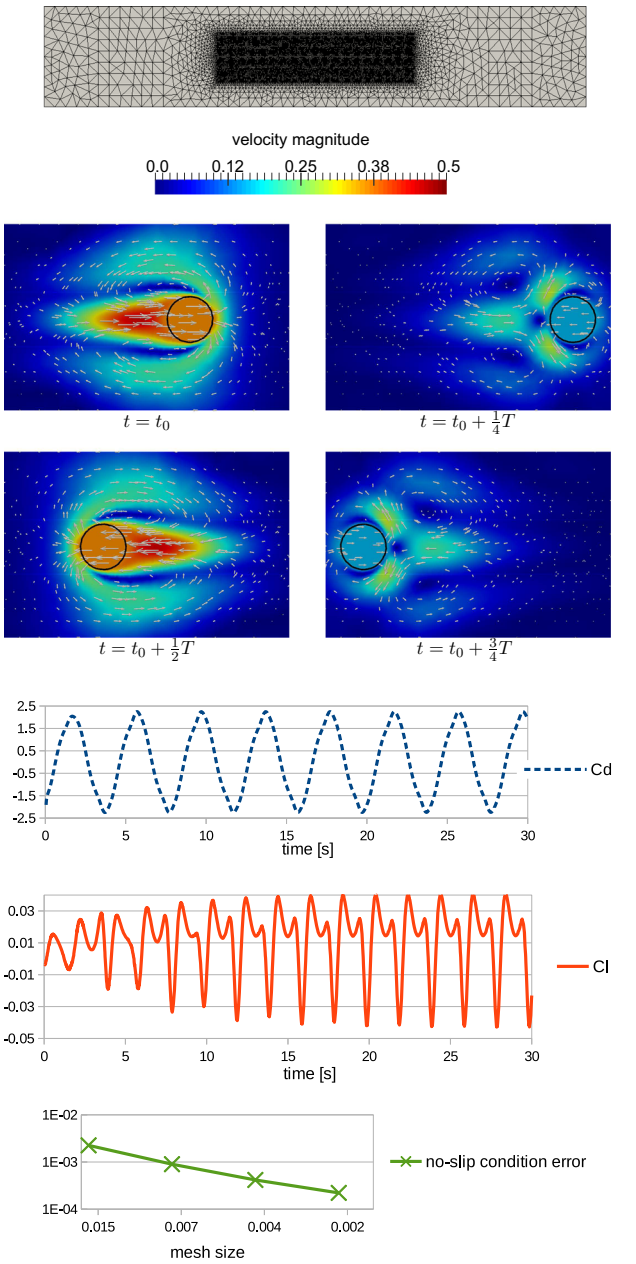

Fig. 12 The oscillating cylinder test (Wan et al. 2004) as benchmark for the RIIS model: on the top the mesh adopted; on the center a zoom on the velocity magnitude with vectors depicted at four instants of the oscillating period ($t_0 = 22.25$ s and $T = 4$ s); on the bottom the resulting drag (C_d, *dotted blue line*) and lift (C_l, *red line*) coefficients and the scaling of the no-slip condition error (*starred green line*) with the mesh size

condition at the boundary of the domain. The complete set of data used in the test are provided in the above reference. Being $(X_c(t), Y_c(t))$ the moving coordinates of the center of the cylinder and $r = 0.05$ its radius, we define the distance function φ from the circumference of the cylinder as:

$$\varphi(x, y, t) = r - \sqrt{(x - X_c(t))^2 + (y - Y_c(t))^2}, \qquad (40)$$

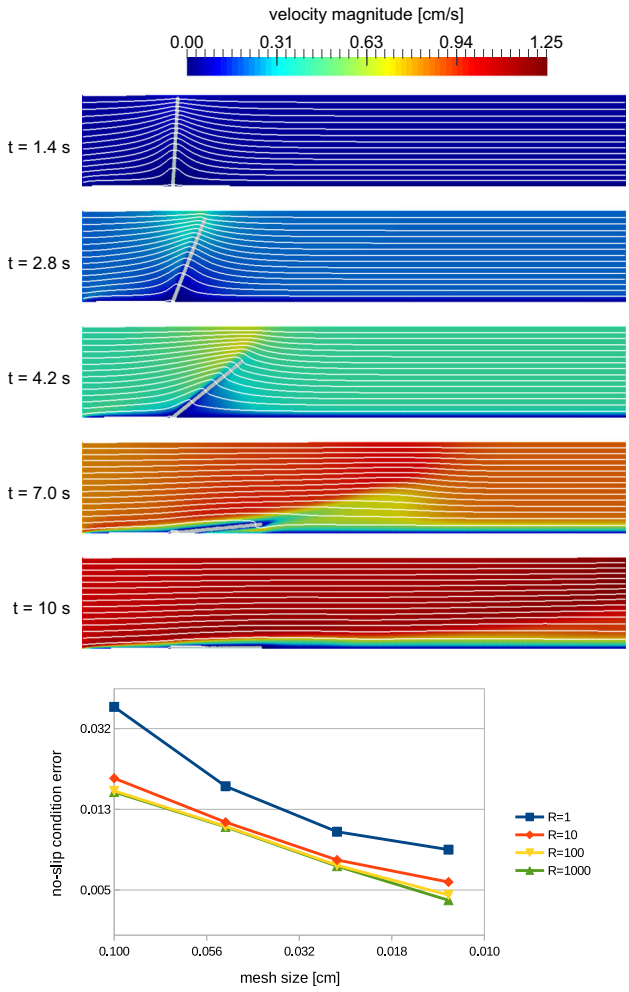

Fig. 13 The valve test (Auricchio et al. 2016) as benchmark for the RIIS model: on the top the velocity magnitude and the streamlines at the same instants shown in the reference paper; on the bottom the scaling of the no-slip condition error with the mesh size for different values of the resistance R_Γ

while the auxiliary level set function ψ can be defined as an arbitrary negative function. We define the smooth Dirac function as:

$$\delta_\varepsilon(\varphi) = 0.5\ (1 + \tanh(2.5\,\varphi/\varepsilon))\,, \tag{41}$$

in order to activate the resistive term also inside the cylinder. We choose a time step of 0.01 s and we generate a non-uniform mesh (Fig. 12, top). We set the resistance R_Γ equal to 200 and the parameter ε equal to $2h$, being $h = 0.004$ the mesh size near the moving cylinder. In Figure 12, center, we show the results of the velocity field at four characteristic instants of the oscillating period, that well compare with the vorticity field shown in (Auricchio et al. 2016). The computed drag (C_d) and lift (C_l) coefficients are highlighted in Fig. 12, bottom. Finally, we define the dimensionless error e in the imposition of the no-slip condition on the immersed body Γ, i.e., the cylinder, as:

$$e = \frac{||\big(1 - \mathcal{H}(\psi)\big)\,\delta_\varepsilon(\varphi)\,(\boldsymbol{u} - \boldsymbol{u}_\Gamma)||_{L^2}}{||\big(1 - \mathcal{H}(\psi)\big)\,\delta_\varepsilon(\varphi)\,U_\Gamma||_{L^2}}, \tag{42}$$

where $\boldsymbol{u}_\Gamma$ and U_Γ are the prescribed velocity of the immersed body and its characteristic value taken as its maximum magnitude in time, respectively. We find an average value in time of $e = 4.16 \times 10^{-4}$, thus demonstrating the fulfillment of the no-slip condition in the cylinder; furthermore, a linear scaling of the error with respect to the mesh size is reported, as shown in Fig. 12, bottom.

The second benchmark problem is reported in Auricchio et al. (2016), where it is specifically referred as Test 2, in which the motion of a rigid body in the fluid, specifically a rigid valve leaflet, is prescribed. In order to reproduce the results, we generate a uniformly distributed mesh characterized by a mesh size $h = 0.0125$ cm and we set the resistance $R_\Gamma = 100$ and the parameter $\varepsilon = 2h$. We define the two level set functions as:

$$\begin{aligned} \varphi(x, y, \vartheta(t)) &= \cos(\vartheta(t))\, y - \sin(\vartheta(t))\, x, \\ \psi(x, y) &= l - \sqrt{x^2 + y^2}, \end{aligned} \tag{43}$$

where ϑ is the prescribed opening angle of the valve and $l = 0.999$ is the length of the leaflet. The velocity of the valve $\boldsymbol{u}_\Gamma$ is determined accordingly using the prescribed value of $\partial\vartheta/\partial t$. For this test, the original smooth Dirac function [Eq. (10)] is used. The results of the test are shown in Figure 13. We find an average value in time of the no-slip condition error $e = 4.47 \times 10^{-3}$, demonstrating again the successfully imposition of the no-slip condition on the immersed surface Γ; we also note a linear scaling of the error with the mesh size h and a reduction of the error with the increasing of the resistance R_Γ that becomes negligible over a certain value (Fig. 13, bottom). Finally, the results obtained for the velocity field (Fig. 13, top) very well agree with those in (Auricchio et al. 2016); albeit qualitative, this comparison provides a validation of our RIIS approach against a benchmark problem in the same area of application.

References

Astorino M, Gerbeau JF, Pantz O, Traoré KF (2009) Fluid–structure interaction and multi-body contact: application to aortic valves. Comput Methods Appl Mech Eng 198(45):3603–3612

Astorino M, Hamers J, Shadden SC, Gerbeau JF (2012) A robust and efficient valve model based on resistive immersed surfaces. Int J Numer Methods Biomed Eng 28(9):937–959

Auricchio F, Conti M, Morganti S, Totaro P (2011) A computational tool to support pre-operative planning of stentless aortic valve implant. Med Eng Phys 33(10):1183–1192

Auricchio F, Conti M, Ferrara A, Morganti S, Reali A (2014) Patient-specific simulation of a stentless aortic valve implant: the impact of

fibres on leaflet performance. Comput Methods Biomech Biomed Eng 17(3):277–285
Auricchio F, Lefieux A, Reali A, Veneziani A (2016) A locally anisotropic fluid–structure interaction remeshing strategy for thin structures with application to a hinged rigid leaflet. Int J Numer Methods Eng 107(2):155–180
Avolio P (1980) Multi-branched model of the human arterial system. Med Biol Eng comput 18(6):709–718
Barber DC, Oubel E, Frangi AF, Hose D (2007) Efficient computational fluid dynamics mesh generation by image registration. Med Image Anal 11(6):648–662
Bazilevs Y, Calo V, Cottrell J, Hughes T, Reali A, Scovazzi G (2007) Variational multiscale residual-based turbulence modeling for large eddy simulation of incompressible flows. Comput Methods Appl Mech Eng 197(1):173–201
Bonomi D, Vergara C, Faggiano E, Stevanella M, Conti C, Redaelli A, Puppini G, Faggian G, Formaggia L, Luciani G (2015) Influence of the aortic valve leaflets on the fluid-dynamics in aorta in presence of a normally functioning bicuspid valve. Biomech Model Mechanobiol 14(6):1349–1361
Borazjani I (2013) Fluid–structure interaction, immersed boundary-finite element method simulations of bio-prosthetic heart valves. Comput Methods Appl Mech Eng 257:103–116
Borazjani I, Ge L, Sotiropoulos F (2010) High-resolution fluid–structure interaction simulations of flow through a bi-leaflet mechanical heart valve in an anatomic aorta. Ann Biomed Eng 38(2):326–344
Caballero A, Laín S (2013) A review on computational fluid dynamics modelling in human thoracic aorta. Cardiovasc Eng Technol 4(2):103–130
Chandra S, Rajamannan NM, Sucosky P (2012) Computational assessment of bicuspid aortic valve wall-shear stress: implications for calcific aortic valve disease. Biomech Model Mechanobiol 11(7):1085–1096
Chandran KB, Vigmostad SC (2013) Patient-specific bicuspid valve dynamics: overview of methods and challenges. J Biomech 46(2):208–216
Charitos EI, Sievers HH (2013) Anatomy of the aortic root: implications for valve-sparing surgery. Ann Cardiothorac Surg 2(1):53
Cheng R, Lai YG, Chandran KB (2004) Three-dimensional fluid–structure interaction simulation of bileaflet mechanical heart valve flow dynamics. Ann Biomed Eng 32(11): 1471–1483
Conti CA, Della Corte A, Votta E, Del Viscovo L, Bancone C, De Santo LS, Redaelli A (2010a) Biomechanical implications of the congenital bicuspid aortic valve: a finite element study of aortic root function from in vivo data. J Thorac Cardiovasc Surg 140(4):890–896
Conti CA, Votta E, Della Corte A, Del Viscovo L, Bancone C, Cotrufo M, Redaelli A (2010b) Dynamic finite element analysis of the aortic root from mri-derived parameters. Med Eng Phys 32(2):212–221
Crosetto P, Deparis S, Fourestey G, Quarteroni A (2011) Parallel algorithms for fluid–structure interaction problems in haemodynamics. SIAM J Sci Comput 33(4):1598–1622
De Hart J, Baaijens F, Peters G, Schreurs P (2003a) A computational fluid–structure interaction analysis of a fiber-reinforced stentless aortic valve. J Biomech 36(5):699–712
De Hart J, Peters G, Schreurs P, Baaijens F (2003b) A three-dimensional computational analysis of fluid–structure interaction in the aortic valve. J Biomech 36(1):103–112
De Hart J, Peters G, Schreurs P, Baaijens F (2004) Collagen fibers reduce stresses and stabilize motion of aortic valve leaflets during systole. J Biomech 37(3):303–311
Della Corte A, Bancone C, Conti CA, Votta E, Redaelli A, Del Viscovo L, Cotrufo M (2012) Restricted cusp motion in right–left type of bicuspid aortic valves: a new risk marker for aortopathy. J Thorac Cardiovasc Surg 144(2):360–369
Deparis S, Forti D, Grandperrin G, Quarteroni A (2016) FaCSI: a block parallel preconditioner for fluid–structure interaction in hemodynamics. J Comput Phys 327:700–718
Faggiano E, Antiga L, Puppini G, Quarteroni A, Luciani GB, Vergara C (2013a) Helical flows and asymmetry of blood jet in dilated ascending aorta with normally functioning bicuspid valve. Biomech Model Mechanobiol 12(4):801–813
Faggiano E, Formaggia L, Antiga L (2013b) An open-source tool for patient-specific fluid–structure vessel mesh generation. In: Fifth international symposium on modelling of physiological flows (MPF), pp 25–26
Fedele M, Faggiano E, Barbarotta L, Cremonesi F, Formaggia L, Perotto S (2015) Semi-automatic three-dimensional vessel segmentation using a connected component localization of the region-scalable fitting energy. In: 9th international symposium on image and signal processing and analysis (ISPA 2015). IEEE, pp 72–77
Fernández MA, Gerbeau JF, Martin V (2008) Numerical simulation of blood flows through a porous interface. ESAIM Math Model Numer Anal 42(06):961–990
Formaggia L, Quarteroni A, Veneziani A (2010) Cardiovascular mathematics modeling and simulation of the circulatory system, vol 1. Springer, Berlin
Forti D, Dedè L (2015) Semi-implicit bdf time discretization of the Navier–Stokes equations with VMS–LES modeling in a high performance computing framework. Comput Fluids 117:168–182
Gauthier A, Saleri F, Veneziani A (2004) A fast preconditioner for the incompressible Navier Stokes equations. Comput Vis Sci 6(2–3):105–112
Ge L, Sotiropoulos F (2007) A numerical method for solving the 3D unsteady incompressible Navier–Stokes equations in curvilinear domains with complex immersed boundaries. J Comput Phys 225(2):1782–1809
Ge L, Sotiropoulos F (2010) Direction and magnitude of blood flow shear stresses on the leaflets of aortic valves: is there a link with valve calcification? J Biomech Eng 132(1):014,505
Griffith BE (2012) Immersed boundary model of aortic heart valve dynamics with physiological driving and loading conditions. Int J Numer Methods Biomed Eng 28(3):317–345
Handke M, Heinrichs G, Beyersdorf F, Olschewski M, Bode C, Geibel A (2003) In vivo analysis of aortic valve dynamics by transesophageal 3-dimensional echocardiography with high temporal resolution. J Thorac Cardiovasc Surg 125(6):1412–1419
Hsu MC, Kamensky D, Bazilevs Y, Sacks MS, Hughes TJ (2014) Fluid–structure interaction analysis of bioprosthetic heart valves: significance of arterial wall deformation. Comput Mech 54(4):1055–1071
Hunt JC, Wray A, Moin P (1988) Eddies, streams, and convergence zones in turbulent flows. Center for Turbulence Research Report CTR-S88, pp 193–208
Kamensky D, Hsu MC, Schillinger D, Evans JA, Aggarwal A, Bazilevs Y, Sacks MS, Hughes TJ (2015) An immersogeometric variational framework for fluid–structure interaction: application to bioprosthetic heart valves. Comput Methods Appl Mech Eng 284:1005–1053
Korakianitis T, Shi Y (2006) Numerical simulation of cardiovascular dynamics with healthy and diseased heart valves. J Biomech 39(11):1964–1982
Laadhari A, Quarteroni A (2016) Numerical modeling of heart valves using resistive Eulerian surfaces. Int J Numer Methods Biomed Eng, 32(5). doi:10.1002/cnm.2743
Le TB, Sotiropoulos F (2013) Fluid–structure interaction of an aortic heart valve prosthesis driven by an animated anatomic left ventricle. J Comput Phys 244:41–62

Leyh RG, Schmidtke C, Sievers HH, Yacoub MH (1999) Opening and closing characteristics of the aortic valve after different types of valve-preserving surgery. Circulation 100(21):2153–2160

van Loon R, Anderson PD, van de Vosse FN (2006) A fluid–structure interaction method with solid-rigid contact for heart valve dynamics. J Comput Phys 217(2):806–823

Marom G (2015) Numerical methods for fluid–structure interaction models of aortic valves. Arch Comput Methods Eng 22(4):595–620

Marom G, Haj-Ali R, Raanani E, Schäfers HJ, Rosenfeld M (2012) A fluid–structure interaction model of the aortic valve with coaptation and compliant aortic root. Med Biol Eng Comput 50(2):173–182

Marom G, Kim HS, Rosenfeld M, Raanani E, Haj-Ali R (2013) Fully coupled fluid–structure interaction model of congenital bicuspid aortic valves: effect of asymmetry on hemodynamics. Med Biol Eng Comput 51(8):839–848

McQueen D, Peskin C (2000) A three-dimensional computer model of the human heart for studying cardiac fluid dynamics. ACM SIGGRAPH Comput Graph 34(1):56–60

Morganti S, Conti M, Aiello M, Valentini A, Mazzola A, Reali A, Auricchio F (2014) Simulation of transcatheter aortic valve implantation through patient-specific finite element analysis: two clinical cases. J Biomech 47(11):2547–2555

Morsi YS, Yang WW, Wong CS, Das S (2007) Transient fluid–structure coupling for simulation of a trileaflet heart valve using weak coupling. J Artif Organs 10(2):96–103

Nestola MGC, Faggiano E, Vergara C, Lancellotti RM, Ippolito S, Filippi S, Quarteroni A, Scrofani R (2016) Computational comparison of aortic root stresses in presence of stentless and stented aortic valve bio-prostheses. Comput Methods Biomech Biomed Eng 20(2):171–181

Osher S, Fedkiw RP (2001) Level set methods: an overview and some recent results. J Comput Phys 169(2):463–502

Pasta S, Rinaudo A, Luca A, Pilato M, Scardulla C, Gleason TG, Vorp DA (2013) Difference in hemodynamic and wall stress of ascending thoracic aortic aneurysms with bicuspid and tricuspid aortic valve. J Biomech 46(10):1729–1738

Peskin CS (1972) Flow patterns around heart valves: a numerical method. J Comput Phys 10(2):252–271

Peskin CS (2002) The immersed boundary method. Acta Numer 11:479–517

Quarteroni A (2014) Numerical models for differential problems, vol 8. Springer, Berlin

Quarteroni A (2015) Modeling the heart and the circulatory system, vol 14. Springer, Berlin

Quarteroni A, Sacco R, Saleri F (2010) Numerical mathematics, vol 37. Springer, Berlin

Ranga A, Bouchot O, Mongrain R, Ugolini P, Cartier R (2006) Computational simulations of the aortic valve validated by imaging data: evaluation of valve-sparing techniques. Interact Cardiovasc Thorac Surg 5(4):373–378

Rinaudo A, Pasta S (2014) Regional variation of wall shear stress in ascending thoracic aortic aneurysms. Proc Inst Mech Eng Part H J Eng Med 228(6):627–638

Sahasakul Y, Edwards WD, Naessens JM, Tajik AJ (1988) Age-related changes in aortic and mitral valve thickness: implications for two-dimensional echocardiography based on an autopsy study of 200 normal human hearts. Am J Cardiol 62(7):424–430

Sigovan M, Hope MD, Dyverfeldt P, Saloner D (2011) Comparison of four-dimensional flow parameters for quantification of flow eccentricity in the ascending aorta. J Magn Reson Imaging 34(5):1226–1230

Sturla F, Votta E, Stevanella M, Conti CA, Redaelli A (2013) Impact of modeling fluid–structure interaction in the computational analysis of aortic root biomechanics. Med Eng Phys 35(12):1721–1730

Taylor CA, Steinman DA (2010) Image-based modeling of blood flow and vessel wall dynamics: applications, methods and future directions. Ann Biomed Eng 38(3):1188–1203

Tricerri P, Dedè L, Deparis S, Quarteroni A, Robertson AM, Sequeira A (2015) Fluid–structure interaction simulations of cerebral arteries modeled by isotropic and anisotropic constitutive laws. Comput Mech 55(3):479–498

Tse KM, Chiu P, Lee HP, Ho P (2011) Investigation of hemodynamics in the development of dissecting aneurysm within patient-specific dissecting aneurismal aortas using computational fluid dynamics (CFD) simulations. J Biomech 44(5):827–836

Van Steenhoven A, Verlaan C, Veenstra P, Reneman R (1981) In vivo cinematographic analysis of behavior of the aortic valve. Am J Physiol Heart Circ Physiol 240(2):H286–H292

Vergara C, Viscardi F, Antiga L, Luciani GB (2012) Influence of bicuspid valve geometry on ascending aortic fluid dynamics: a parametric study. Artif Organs 36(4):368–378

Wan D, Turek S, Rivkind LS (2004) An efficient multigrid fem solution technique for incompressible flow with moving rigid bodies. In: Feistauer M, Dolejší V, Knobloch P, Najzar K (eds) Numerical mathematics and advanced applications. Springer, Berlin, pp 844–853

Wendell DC, Samyn MM, Cava JR, Ellwein LM, Krolikowski MM, Gandy KL, Pelech AN, Shadden SC, LaDisa JF (2013) Including aortic valve morphology in computational fluid dynamics simulations: initial findings and application to aortic coarctation. Med Eng Phys 35(6):723–735

Yang Y, Li C, Kao CY, Osher S (2010) Split bregman method for minimization of region-scalable fitting energy for image segmentation. In: Bebis G, Boyle R, Parvin B, Koracin D, Chung R, Hammound R, Hussain M, Kar-Han T, Crawfis R, Thalmann D, Kao D, Avila L (eds) Advances in visual computing. Springer, Berlin, pp 117–128